IMMUNOLOGY

Mechanotransduction governs CD40 function and underlies X-linked hyper-IgM syndrome

Hyun-Kyu Choi[1,2,3]†, Stefano Travaglino[1,2]†, Matthias Münchhalfen[4], Richard Görg[4], Zhe Zhong[1,5], Jintian Lyu[1], David M. Reyes-Aguilar[1], Jürgen Wienands[4], Ankur Singh[1,2,5], Cheng Zhu[1,2,5]*

B cell maturation depends on cognate interactions between the T and B cells. Upon interaction with CD40 ligand (CD40L) on T cells, CD40 delivers costimulatory signals alongside B cell antigen receptor (BCR) signaling to regulate affinity maturation and antibody class switch. Mutations affecting CD40-CD40L interactions cause abnormal antibody responses in immunodeficiencies known as X-linked hyper-IgM syndrome (X-HIgM). Here, we study the CD40-mediated mechanotransduction in B cells, which likely occurs during their physical contacts with T cells. We found that CD40 forms catch bond with CD40L that lasts longer at larger forces, both B and T cells exert tension on CD40-CD40L bonds, and force enhances CD40 signaling and antibody class switch. X-HIgM CD40L mutations impair catch bond formation, suppress endogenous tension, and reduce force-enhanced CD40 signaling, leading to deficiencies in antibody class switch. Our findings highlight the role of mechanotransduction in CD40 function and provide insights into the mechanisms underlying X-HIgM syndrome.

INTRODUCTION

As a key costimulatory receptor on B cells, CD40 delivers complementary signals alongside B cell antigen receptor (BCR) signaling to prevent B cell silencing or deletion (*1*–*3*). Upon binding to the BCR, a thymus-dependent (TD) antigen is internalized by the B cell and the processed peptides are presented by major histocompatibility complex (pMHC) molecules on the cell surface. This TD antigen is tested by the T cell receptor (TCR) of follicular T helper (T_{FH}) cells in a process known as linked recognition (*4*, *5*). Upon recognition of the TD antigen, the T_{FH} cell is activated to express a costimulatory ligand, CD40L (CD154) (*6*), which binds CD40 on B cells. Such binding induces CD40 signaling to activate the noncanonical nuclear factor κB (NF-κB) pathway (*7*), promoting B cell activation and their terminal differentiation into antibody-secreting plasma cells (*8*, *9*). In addition to CD40 signaling, multiple cytokines regulate B cell response and differentiation, including B cell activating factor (BAFF), produced by follicular dendritic cells (FDCs) (*8*), and interleukin-4 (IL-4) and IL-21, secreted by T_{FH} cells (*10*). B cells, FDCs, and T_{FH} cells form germinal centers (GCs) where B cells undergo proliferation and somatic hypermutation (*11*) to generate B cell clones expressing BCRs of variable antigen affinities to be selected by a process known as affinity maturation. Another important process occurring in GC is immunoglobulin (Ig; or antibody) class switch recombination (CSR) by which B cells exchange the surface Ig isotype from IgM to other Ig classes, i.e., IgG, IgE, or IgA, which have different immune effector functions and tissue distributions (*12*, *13*).

Affinity maturation and CSR of GC B (GCB) cells require signaling induced by the cross B-T intercellular junctional CD40-CD40L interaction, which also generates a survival signal to prevent B cell apoptosis induced by the BCR signal alone (*14*). B cells repeatedly migrate between the dark and light zones of GCs to take up cognate antigens from FDCs and present the proteolytic peptide products via MHC class II to T_{FH} cells, thereby initiating the CD40-CD40L costimulatory signaling axis (*15*–*17*). In the absence of this interaction, B cells undergo apoptosis, allowing for the selection of B cell clones with a high-affinity BCR (*15*, *16*).

Various genetic defects that hinder the ability of B cells to undergo CSR and lead to abnormal antibody responses have been discovered, together making up a class of immunodeficiencies known as X-linked hyper-IgM syndrome (X-HIgM) (*18*–*23*). The most common defects leading to X-HIgM are mutations to the CD40L protein itself (X-HIgM type I) that affect its expression, binding, or function (*18*, *19*, *24*), resulting in dysregulated signaling in B cells and their inability to undergo CSR (*19*). Other defects include the enzymes involved in CSR, such as activation-induced cytidine deaminase (*21*) and uracil-DNA glycosylase (*22*). The inability of X-HIgM patients' B cells to undergo class switches from IgM to the IgG, IgA, or IgE isotypes renders them partially immunodeficient, unable to generate lasting immune memory to pathogens, and prone to recurring bacterial, fungal, or viral infections (*18*, *23*, *25*). Among the numerous possible mutations to CD40L, missense mutations are of high interest because they affect CD40-CD40L binding rather than trivially abrogating expression (*24*); therefore, studying these mutations can help understand CD40 signaling and function.

B cell CD40 is a category II tumor necrosis factor receptor (TNFR). Unlike category I TNFRs (named after TNFR1), which can be activated by soluble TNF ligands (TNFLs), category II TNFRs required membrane-bound TNFLs to be fully activated (*26*–*28*), which is the case for CD40 (*26*). Furthermore, it has been reported that the potency for soluble CD40L to activate CD40 increased ~25 times by fusing CD40L with an antibody single-chain variable fragment against a tumor surface marker to provide a membrane anchor (*29*, *30*). Moreover, it has been observed that substrate stiffness plays a role in CD40 function, with anti-CD40 functionalized on stiffer substrates leading to enhanced B cell proliferation (*31*). As both soluble and membrane CD40L share the same TNF homology domain (THD) that interacts with CD40, their differential functionalities cannot be attributed to

[1]Wallace H. Coulter Department of Biomedical Engineering, Georgia Institute of Technology and Emory University, Atlanta, GA 30332, USA. [2]Parker H. Petit Institute for Bioengineering and Biosciences, Georgia Institute of Technology, Atlanta, GA 30332, USA. [3]Department of Biochemistry, College of Life Science and Biotechnology, Yonsei University, Seoul 03722, South Korea. [4]Institute of Cellular and Molecular Immunology, University Medical Center Göttingen, 13 Göttingen, Germany. [5]George W. Woodruff School of Mechanical Engineering, Georgia Institute of Technology, Atlanta, GA 30332, USA.
*Corresponding author. Email: cheng.zhu@bme.gatech.edu
†These authors contributed equally to this work.

protein sequence-encoded information. Conceptually, due to the migratory nature of both B and T cells during their encounters and the subsequent formation of T-B immunological synapses where relative sliding between two cell membranes occurs against the resistance of cross-junctional interactions, there should be ample opportunities for engaged receptor-ligand bonds to experience mechanical forces (*32*). Not only T (or B) cells can provide mechanical support to resist forces coming from the B (or T) cells, but also B, T, or both cells may also generate forces, both of which act on CD40-CD40L bonds. By comparison, there must not necessarily be mechanical forces on CD40 bound with soluble CD40L. Therefore, we hypothesize that CD40 functions as a mechanoreceptor and mechanosensor to receive and sense force-modulated signals from CD40L. We further hypothesize that X-HIgM CD40L mutations dysregulate mechanosignaling of CD40 despite its ability to bind CD40L, thereby contributing to the disease. To test these hypotheses, we deployed a battery of biophysical techniques to characterize CD40's mechanosensing properties and investigate how dysregulation of CD40 mechanotransduction by X-HIgM CD40L mutations may affect B cell signaling and function.

RESULTS

Force-free 2D kinetics of CD40-CD40L interactions

So far, studies on the binding of CD40L to CD40 has been limited to measuring soluble protein ectodomain interactions in the fluid phase (*33*), i.e., three-dimensional (3D) binding (*34*). To better mimic the physiological situation in which the interacting proteins that are expressed as membrane-bound molecules on the surfaces of two apposing cells, we apply our mechanical-based adhesion frequency assay to measure CD40-CD40L interactions across two solid surfaces, i.e., 2D binding (*34*–*37*). These two types of binding are so-called because the affinities of 3D and 2D binding have different dimensions, volume in 3D and surface in 2D.

To measure 2D binding, we first produced wild-type (WT) N-terminally biotinylated CD40L ectodomain protein and five X-HIgM–related mutants (S132W, E142G, K143A, R207A, and A208D) (Fig. 1A) using a human embryonic kidney (HEK) cell mammalian expression system, which were purified and confirmed by polyacrylamide gel electrophoresis (PAGE) and immunocytometry (fig. S1, A and B). Of these, A208D is found in X-HIgM patients (*38*), K143A is closely related to the K143T mutant found in patients (*39*, *40*), and S132W was chosen from mutagenesis screening as a control mutation, since A208D and K143A share a similar property of neutralizing the positive charge and S132W is located away from the CD40-CD40L binding site (Fig. 1A) (*41*). We also added to our study two more mutants, E142G and R207A, which are located one amino acid distal from the natural variants, to test whether charged interactions local to the CD40 and CD40L binding interface are necessary for productive binding (*24*, *42*) and affect CD40 mechanotransduction (Fig. 1A).

Using these soluble CD40L proteins, we performed the adhesion frequency assay (*35*) using a biomembrane force probe (BFP) (*43*, *44*). A BFP employs a micropipette-aspirated human red blood cell (RBC) with a CD40L-bearing bead (probe) attached to its apex to act as a force sensor for detecting binding to a CD40-bearing bead (Fig. 1B) or a B cell (Fig. 1C) (target) aspirated by an opposing micropipette (fig. S1C) (*37*). The adhesion frequency (P_a = # of binding events divided by # of contacts) was measured by repeated contact cycles for each probe-target pair, obtaining mean $P_a \pm$ SEM as a function of contact time (t_c) using four to five probe-target pairs per t_c value. To examine the kinetics of the interaction and directly compare among different CD40L constructs, we converted the contact time-dependent P_a values to the average number of bonds per contact, $\langle n \rangle = -\ln(1 - P_a)$, based on the Poisson distribution of bonds (*35*), normalized them by the densities of both CD40 (m_{CD40}) and CD40L (m_{CD40L}), and plotted the resulting normalized bond number ($\langle n \rangle / m_{CD40} m_{CD40L}$) versus t_c for CD40L-coated beads (fig. S1D) and CD40-expressing peripheral blood mononuclear cell (PBMC)–derived B cells (Fig. 1D) or GC-line B cell lymphoma (GCB lymphoma) Farage B cells (Fig. 1E). We then fitted such data by a kinetic model (*35*), $\langle n \rangle / m_{CD40} m_{CD40L} = A_c K_{a,} 0(1 - e^{-k_{off,0}t_c})$, to obtain an "apparent" effective zero-force 2D affinities ($A_c K_{a,0}$) and zero-force off-rates ($k_{off,0}$) of WT CD40L and X-HIgM mutants for the CD40 ectodomain coated on beads (Fig. 1, F and G) and for CD40 expressed on the B cell membrane (Fig. 1H and fig. S1E). The bead-bead experiments (Fig. 1B) rule out any possible confounding factors related to cellular and membrane processes involving CD40 (e.g., receptor diffusion and clustering on the cell surface) that may be present in the bead-cell experiments (Fig. 1C). In the adhesion frequency assay, the contact area size was kept constant for the same system but could vary among different systems. For this reason, the contact area A_c is not separable from the affinity $K_{a,0}$ and is therefore explicitly expressed as the product of the two ($A_c K_{a,0}$). Despite that the contact area A_c might vary from system to system, the consistencies among WT $A_c K_{a,0}$ values in Fig. 1 (F and H) obtained from different systems indicate that the measurements on B cell surface are not confounded by such factors.

Remarkably, soluble CD40 showed reduced $A_c K_{a,0}$ values for both $CD40L^{K143A}$ and $CD40L^{A208D}$ compared to $CD40L^{WT}$ and reduced off-rate from $CD40L^{K143A}$ but not from $CD40L^{A208D}$ (Fig. 1, F and G). The X-HIgM mutants led to 2.2- and 2.6-fold (S132W), 2.6- and 1.8-fold (E142G), 37- and 8.2-fold (K143A), and 17- and 7.8-fold (R207A) reductions in $A_c K_{a,0}$ for CD40 on PBMC and Farage B cells, respectively (Fig. 1H), as well as few fold off-rate variations (fig. S1E) compared to $CD40L^{WT}$.

CD40 forms catch bonds with CD40L that are suppressed or eliminated by X-HIgM mutations

The apparent effective 2D affinities and off-rates shown in Fig. 1 (F to H) and fig. S1E were measured under the force-free condition by nature of the adhesion frequency assay (*35*), which is indicated by the subscript 0. We next asked whether and, if so, how force affects the dissociation kinetics of CD40-CD40L bonds. To address this question, we used BFP to load single CD40-CD40L bonds with precisely controlled forces and measured the bond lifetimes under a range of constant forces (fig. S1C). $CD40L^{WT}$ formed a catch-slip bond with CD40, where lifetime increases with increasing force up to ~15 pN (optimal force) and then decreases with further increase in force; this held true for both PBMC and GCB lymphoma Farage B cells (Fig. 1, I and J, both with WT CD40L), suggesting that the dissociation of CD40-CD40L bond is modulated by force. This is intriguing because catch bonds have also been observed in several immunoreceptors, for instance, the TCR forms catch bonds with agonist pMHCs (*45*–*47*). Intuitively, catch bonds enable force to prolong engagement time and stabilize interacting molecular complexes, which may allow sufficient time for downstream biological processes to proceed as needed, potentially resulting in more protein docking and conformational changes, more enzymatic modifications, formation of more molecular assemblies

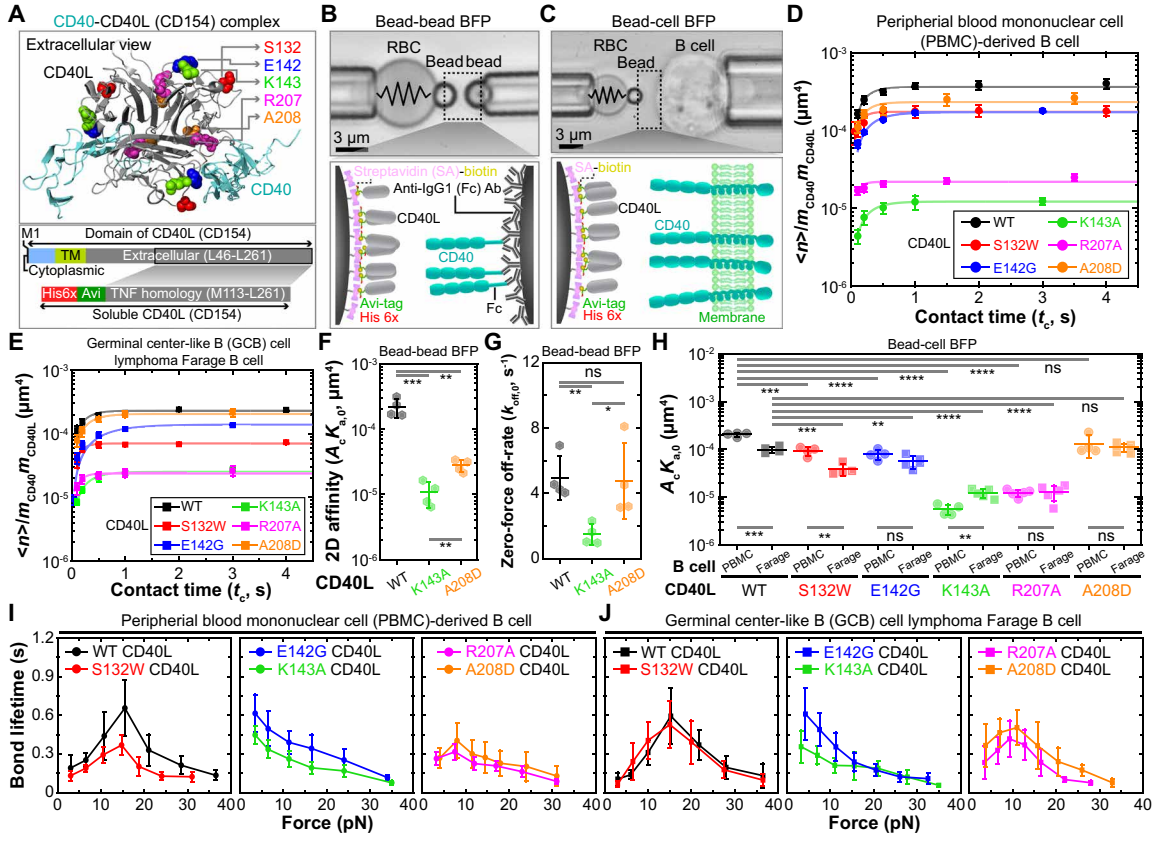

Fig. 1. Measuring kinetic parameters of CD40-CD40L interactions. (**A**) Crystal structure of the CD40-CD40L complex ectodomains (top, PDB 3QD6, with X-HIgM type I–related residues highlighted) and diagram of soluble CD40L (bottom). (**B** and **C**) Photomicrographs of BFP setups for bead-bead (B) and bead-cell (C) assays. A CD40L-functionalized bead is attached to a micropipette-aspirated RBC (left) via biotin-streptavidin (SA) coupling (upper). The RBC-bead assembly acts as a force sensor (= spring) to detect CD40L binding with CD40 coated on another bead (B) or expressed on a B cell (C) aspirated by an opposite pipette (right). Scale bar, 3 μm. (**D** and **E**) Mean ± SEM of average number of bonds per contact ($\langle n \rangle$) normalized by CD40 (m_{CD40}) and CD40L (m_{CD40L}) densities versus contact time (t_c). $\langle n \rangle$ [= ln $(1 - P_a)^{-1}$] was converted from the adhesion frequency (P_a = # binding events ÷ total # of contacts) directly measured with CD40L on BFP beads interacting with CD40-expressing PBMC (D) or Farage (E) B cells. Data (points, $n = 4$ to 5) were fitted by a published model (*35*): $\langle n \rangle / m_{CD40} m_{CD40L} = A_c K_{a,0} (1 - e^{-k_{off,0} t_c})$. (**F** to **H**) Mean ± SD of zero-force effective 2D affinity ($A_c K_{a,0}$) [(F) and (H) and off-rate ($k_{off,0}$) (G) obtained from the bead-bead [(F) and (G)] and bead-cell (H) assays. Scatters indicate individual data from each bead-bead ($n = 4$) or bead-cell ($n = 4$ to 5) pairs. Two-sided *t* test was used to assess significance. (**I** and **J**) Mean ± SEM of bond lifetime versus force ($n > 35$ lifetime measurements per force bin) of CD40L-coated beads interacting with CD40-expressing PBMC (I) or Farage (J) B cells using the BFP force-clamp assay [(C) and fig. S1C]. Different panels are categorized by the different types of bonds: catch-slip for WT and S132W (left), slip-only for E142G and K143A (middle), and suppressed catch-slip for R207A and A208D (right).

(e.g., signalosomes, biomolecular condensates, and focal adhesions), and possibly others.

Remarkably, X-HIgM mutations to the CD40L binding site (Fig. 1A) either greatly suppressed the extent of catch bonds (Fig. 1, I and J, R207A and A208D) or completely abrogated them, turning the CD40-CD40L interaction into slip-only bonds (Fig. 1, I and J, E142G and K143A); again, these results held true for both PBMC and Farage B cells, suggesting that X-HIgM mutations adversely affect the force modulation of CD40-CD40L bond dissociation, which may translate into dysregulation of CD40 signaling and downstream biological processes. The $CD40L^{S132W}$ mutation distal to the binding site (Fig. 1A) lowered the extent of catch bond in PBMC B cells (Fig. 1I, S132W) but not in Farage B cells (Fig. 1J, S132W). Since for exponentially distributed lifetimes common for single-bond dissociation, average bond lifetime equals reciprocal off-rate (*48*), we plotted the reciprocal zero-force off-rates measured from the adhesion frequency experiment versus the bond lifetimes measured at the lowest force bin by the force-clamp experiment, finding excellent correlation (Fig. 1, I and J, and fig. S1, E and F), thus further confirming the short lifetimes of the catch-slip bonds (WT, S132W, R207A, and A208D) and the long lifetimes of the slip-only bonds (E142G and K143A) at low forces. It is informative that this change in bond type with the CD40L constructs tested was observed not only for membrane CD40 on the B cell surface but also for soluble CD40 ectodomain (fig. S1G), implying that the CD40-CD40L catch bond is governed by ectodomain interactions between CD40 and CD40L.

CD40 experiences cell-generated forces upon engaging immobilized CD40L, which are suppressed by X-HIgM mutations

While the CD40-CD40L catch bond was demonstrated by loading the bond with exogenous forces, B cells have been observed to exert endogenous forces on BCR (*49*–*51*). We, therefore, asked whether CD40 experiences B cell–generated forces upon engagement with

surface-bound CD40L in the range where the catch bond was observed. To answer this question, we used DNA-based molecular tension probes (MTPs) (*52*). An MTP consists of a DNA hairpin that unfolds at a desired tension designed by adjusting the length and guanine-cytosine content of the DNA sequence and is flanked by a fluorophore-quencher pair. One end of the hairpin is functionalized with a CD40L, anti-CD40 (positive control), or bovine serum albumin (BSA) (negative control) molecule, and the other end is linked to a gold nanoparticle (AuNP)–coated surface (Fig. 2A). If a B cell placed on the MTP surface exerts tension on a CD40-CD40L bond (F_{Cell}) that is greater than the DNA hairpin force threshold ($F_{1/2}$), the hairpin would (have a 50% chance to) unfold, separating the quencher (BHQ2) from the fluorophore (Atto647), thus generating a fluorescent signal to report a force of $F_{Cell} > F_{1/2}$ on the bond (Fig. 2A). Adding a single-stranded DNA (ssDNA) (locker) complementary to the unfolded hairpin, which hybridizes with it and locks it in the open configuration after bond dissociation or force removal, allows the fluorescent signal to accumulate (*53*).

Using this technique, we observed that at steady state, both PBMC (Fig. 2B) and Farage (Fig. 2C) B cells efficiently spread on WT CD40L-functionalized MTP surfaces with $F_{1/2}$ of 4.7, 12, and 19 pN and exerted endogenous tensions F_{Cell} above 4.7 pN but below 19 pN (Fig. 2, B to G, and fig. S2, A to J). Transiently, we observed that B cells concurrently spread and applied >4.7-pN force on CD40L as soon as the cells interacted with the surface, rapidly increasing in the first ~8 min, and approached a plateau in 10 to 12 min (fig. S2, K and L, and movie S1). By comparison, when B cells were placed on X-HIgM CD40L mutant–tagged MTP surfaces, their steady-state spreading area and cumulative tension signals were significantly lower at all $F_{1/2}$ levels regardless of the cells tested (Fig. 2, B to I, and fig. S2, A to J). On MTP surfaces of $F_{1/2} = 4.7$ pN, PBMC and Farage B cells generated 7.2- and 11.1-fold less tension signals on $CD40L^{K143A}$ and 8.8- and 19.5-fold less tension signals on $CD40L^{A208D}$, respectively. To directly compare the tension signals measured using MTPs of different $F_{1/2}$ values tagged by different CD40 binding molecules, we normalized all tension signals by that measured using MTP of $F_{1/2} = 4.7$ pN tagged by $CD40L^{WT}$ (Fig. 2, H and I). For PBMC and Farage B cells on $CD40L^{WT}$ MTPs, the >12-pN tension signals decreased by 19.5% and 25%, respectively, whereas the >19-pN tension signals dropped by 74% and 68%, respectively, compared to the >4.7-pN tension signal (Fig. 2, H and I). Thus, B cells are more likely to exert 12 pN < F_{Cell} < 19 pN endogenous forces on CD40 than outside this force range. This suggests a match of the active tension to the force where the lifetime of the CD40-$CD40L^{WT}$ bond peaks as it transitions from the catch regime to the slip regime (i.e., optimal force). By comparison, the tension signals of our positive control (anti-CD40) decreased precipitately with the MTP $F_{1/2}$ from 4.7 to 12 and 19 pN (Fig. 2, H and I), which correlates with the slip-only behavior of the CD40–anti-CD40 bond (fig. S2, M and N).

To explore the origins of such intrinsic force, we treated Farage cells with latrunculin A to depolymerize actin filament (*54*), Y-27632 to inhibit Rock (*55*), and blebbistatin to inhibit myosin IIA (*56*), observing significant reductions in cell spreading and tension signals (fig. S2, O and P), suggesting that these forces are CD40 induced, signaling dependent, and actin-myosin powered (see also the next section).

These data are remarkable, as they suggest a potential mechanobiological mechanism in which CD40 and/or CD40L may be evolved to enable the formation of a catch-slip bond with the force where the bond lifetime peaks to match the endogenous force generated by the cell's cytoskeleton and motor machinery. To test whether B cells were the sole provider of force on CD40-CD40L bonds or T cells might also contribute, we performed an experiment with an inverted configuration by placing human tonsil–derived primary ($CD4^+CXCR5^+PD1^+$) T_{FH} cells and Jurkat T cells, stimulated with inactivated H1N1 antigen or anti-CD3, respectively, to induce CD40L expression, on 4.7-pN MTP tagged with soluble CD40 protein. Both cells spread and applied tension on CD40-CD40L bonds at significantly higher levels than the BSA control (fig. S3), indicating that exogenous tension applied by T cells on CD40L may also have a role in CD40 mechanotransduction.

Endogenous force supports B cell spreading on CD40L, and limiting force suppresses CD40 signaling

Given our finding that B cells generated forces on CD40-CD40L bonds that match their force-dependent dissociation kinetics, we asked whether such endogenous forces are important to CD40-mediated B cell signaling and function. To address this question, we capped the force magnitude that a B cell could exert on any single CD40 molecule and assessed the ability of B cells to spread on CD40L and signal. This was done using the tension gauge tether (TGT) technology (*57*). TGT is similar to MTP in that both take advantage of the property of double-stranded DNA (dsDNA) oligos to dissociate above a tunable force threshold (Fig. 3A). However, MTP is an ssDNA that folds into a hairpin structure, unfolds by an above threshold force, and refolds reversibly after force removal unless another complementary ssDNA hybridizes with the unfolded hairpin to lock it in the open configuration (Fig. 2A). By comparison, TGT uses dsDNA with open ends, hence will rupture irreversibly by above threshold forces (Fig. 3A).

Given our measured bond lifetime versus force curves (Fig. 1, I and J), we chose two TGT designs that detach at threshold forces of 12 and 56 pN, determined by their unzipping and shearing rupture modes, respectively (Fig. 3A) (*57*). When Farage cells were placed on 56-pN TGT surfaces functionalized with $CD40L^{WT}$, allowing up to 56-pN endogenous forces to exert on CD40-CD40L bonds, the cells spread nicely (Fig. 3, B and C). In contrast, when the TGT threshold force was lowered to prevent >12-pN force on CD40-CD40L bonds, cell spreading was greatly reduced, indicating that force is important for B cell spreading on CD40L. Compared to WT, X-HIgM mutations to CD40L failed to support appreciable spreading of Farage cells, showing statistically indistinguishable spreading areas on $CD40L^{K143A}$-functionalized 12- and 56-pN TGTs but significantly smaller spreading areas on $CD40L^{A208D}$-functionalized 12- than 56-pN TGT (Fig. 3, B and C).

B cells spread on FDCs to capture membrane-bound antigens (*58*) and on T_{FH} cells to form immunological synapse (*59*), both of which are important (*60*). Cell spreading has an active component that involves signaling (*61*–*63*). As a first step toward identifying specific molecules downstream of CD40 signaling that might be regulated by B cell endogenous forces on CD40, we developed a bead-based TGT assay coupled with flow cytometry (Fig. 3D) to measure phosphorylation of p38 and extracellular signal–regulated kinase 1/2 (Erk1/2), two kinases known to be important parts of CD40-induced signaling pathways (*42*, *64*–*66*). B cells were coincubated with 12-μm-diameter beads functionalized with CD40L-tagged 12- or 56-pN TGTs, and subsequently harvested at different time points to measure phosphorylation of p38 and Erk1/2. We chose

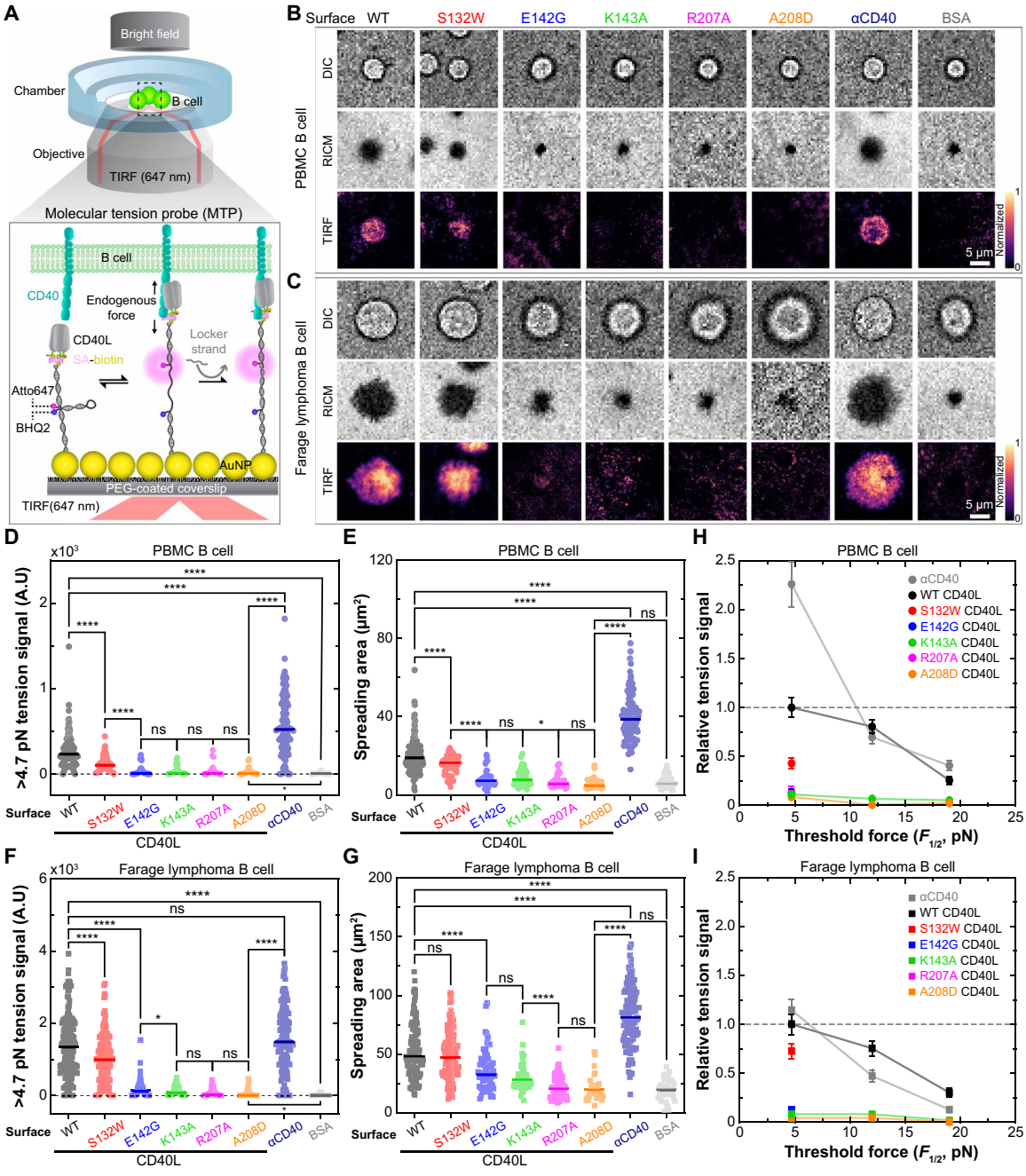

Fig. 2. CD40 experiences B cell–generated forces upon engaging immobilized CD40L, which are suppressed by X-HIgM mutations. (**A**) Schematics of MTP setup (*52*). Top: CD40 on B cells interacts with MTP-tagged CD40L to exert tension on the CD40-CD40L bonds (F_{Cell}). Bottom: A DNA hairpin flanked by a fluorophore (Atto647) and quencher (BHQ2) pair is linked to a CD40L at one end (or an anti-CD40 antibody for positive control, BSA for negative control) and to a gold nanoparticle bound to a PEG-coated glass surface at the other end. If F_{Cell} is greater than the force threshold ($F_{1/2}$) of the DNA hairpin (which depends on its sequence), the hairpin unfolds, dequenching Atto647 and generating a fluorescent signal. A complementary ssDNA (locker) prevents the open hairpin from closing after bond dissociation and force removal, allowing signal accumulation (*53*). (**B** and **C**) Representative images of differential interference contrast microscopy (DIC; first row), reflection interference contrast microscopy (RICM, second row), and total internal reflection fluorescence microscopy (TIRF, third row) from CD40 of PBMC (B) and Farage B cell (C) interacting with indicated CD40L constructs, anti-CD40 antibody, and BSA-tagged MTP surface. Scale bar, 5 μm. (**D** to **G**) Mean and individual data points of >4.7-pN tension signal measured as normalized fluorescence intensity integrated over cell contact area [(D) and (F)] and spreading areas [(E) and (G)] of PBMC [(D) and (E)] and Farage [(F) and (G)] B cells ($n = 25$ to 200) on MTP functionalized with CD40L constructs. Significance was assessed by two-sided *t* test. (**H** and **I**) Mean ± SEM of relative tension signals obtained from placing PBMC (H) and Farage (I) B cells on the indicated CD40L-tagged MTP surfaces. Tensions are normalized by those of >4.7-pN MTP conjugated with $CD40L^{WT}$ to obtain relative values ($n = 25$ to 262 cells).

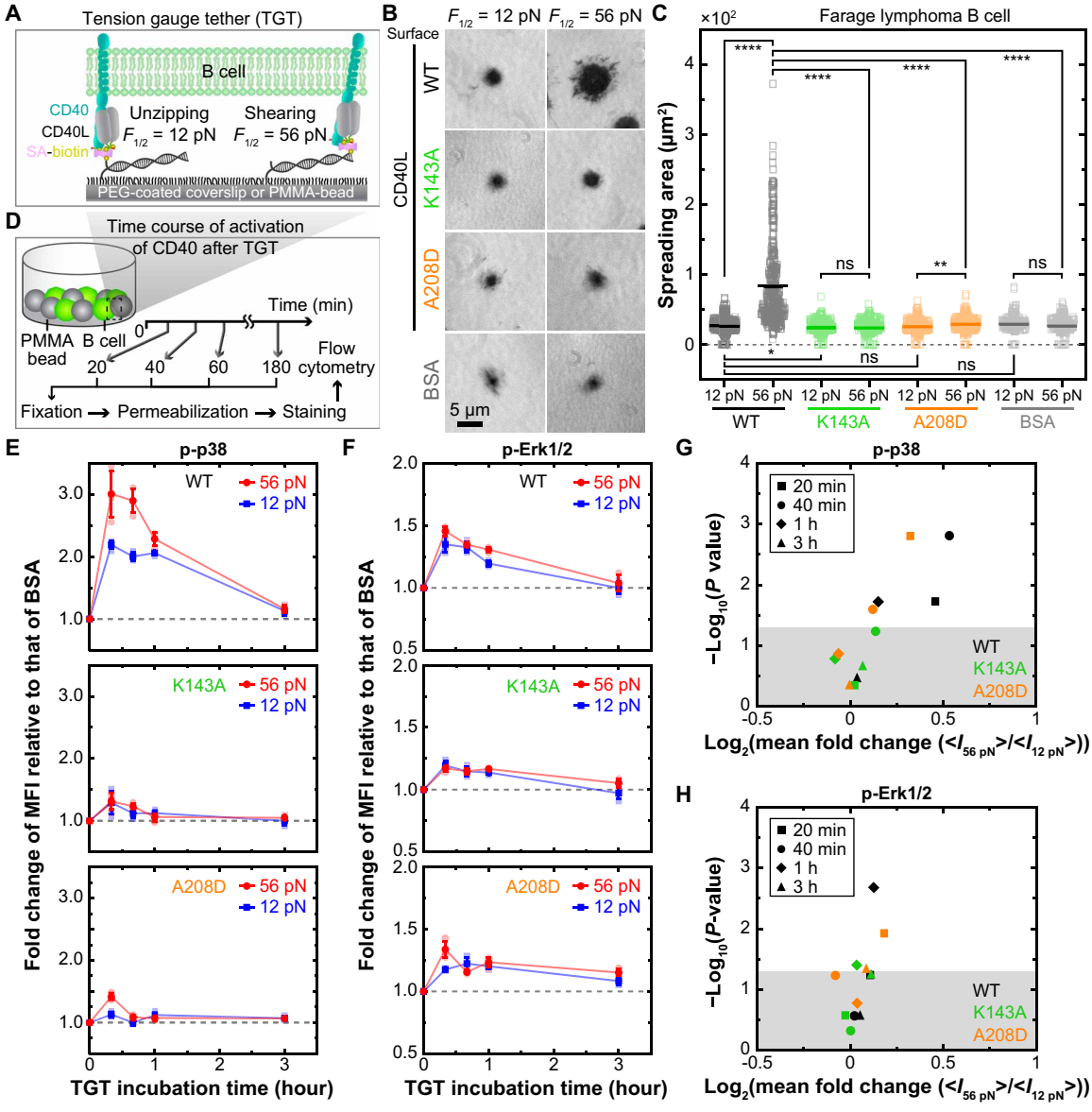

Fig. 3. Endogenous forces support B cell spreading on CD40L and limiting force suppresses CD40 signaling, and X-HIgM mutations impair this phenotypical difference. (**A**) Schematic of conventional TGT setup. A TGT consists of an open-ended dsDNA with one strand linked to a PEG-coated surface and the other tagged to a CD40L. If F_{Cell} on a CD40-CD40L bond exceeds the designed threshold ($F_{1/2}$), the dsDNA dissociates, limiting the force that CD40 can experience. TGT's $F_{1/2}$ depends both on the dsDNA sequence and on the dissociation mode. Linking the dsDNA to the surface and to CD40L in cis (left) versus in trans (right) forces dissociation by different modes, i.e., "unzipping" ($F_{1/2}$ = 12 pN) versus "shearing" ($F_{1/2}$ = 56 pN). (**B**) Representative RICM images of Farage cells spreading on 12- or 56-pN TGTs tagged with indicated CD40L constructs or BSA. Scale bar, 5 μm. (**C**) Mean and individual points (n = 116 to 309) of Farage cells spreading areas on functionalized TGT surfaces. Significance was assessed by two-sided t test. (**D**) Schematic of bead-based TGT for measuring the effect of limiting force on intracellular signaling. Azide-PMMA [poly(methacrylic acid)] beads are functionalized by CD40L (or BSA control)–tagged TGT. B cells cocultured with TGT beads are then analyzed by flow cytometry. (**E** and **F**) Mean ± SD and individual points (N = 3 with n > 10,000 cells) of fold change of PE MFI normalized by that of BSA for phopho-p38 (p-p38) (E) and phospho-Erk1/2 (p-Erk1/2) (F) in Farage cells stimulated with TGT-tagged CD40L constructs are plotted versus incubation time. (**G** and **H**) Log plots of P value versus mean fold change of MFI of p-p38 (G) and p-Erk1/2 (H) between Farage cells stimulated by TGT with 12- and 56-pN force thresholds. Region above shaded area represents P < 0.05.

p38 and Erk1/2 for their role in the regulation of cytokine and chemokine productions (IL-10, IL-12) affecting immune response, class-switch recombination, CD40-induced B cell proliferation, and selection (*66*–*68*). Of note, the size of beads functionalized with TGT should be similar or even larger than the cell size to instigate a contact area for maximal interactions. The phosphorylation of both intracellular molecules showed a biphasic time course that peaked at ~20 min, with levels at all time points higher when Farage cells were allowed to exert up to 56-pN forces on CD40-CD40L bonds than when the forces were capped to <12 pN (Fig. 3, E and F, and fig. S4A). The differences in p38 phosphorylation were significant at 20, 40, and 60 min (Fig. 3, E and G). Erk1/2 phosphorylation showed less pronounced changes and was significantly reduced by <12-pN relative to <56-pN TGT at 60-min time point only (Fig. 3, F and H,

and fig. S4A). Thus, force differentially affects p38 and Erk1/2 signaling, with the p38 pathway more dependent on force than the Erk1/2 pathway. Trends equivalent to those described above for Farage B cells were also observed for PBMC B cells (fig. S4, B to F), indicating that these results are not artifacts of lymphoma cells.

Consistent with their suppressed force-dependent kinetics (Fig. 1, I and J) and their inability to exert higher forces (Fig. 2, B to G, and fig. S2, A to J), phosphorylation of p38 and Erk1/2 for cells incubated with TGTs tagged with X-HIgM CD40L mutants was greatly reduced, with CD40L^{K143A} (which forms a slip-only bond with CD40) being reduced more than CD40L^{A208D} (which forms a suppressed catch-slip bond with CD40) (Fig. 3, E to H, and fig. S4). Also, no significant differences in phosphorylation time courses of p38 and Erk1/2 were detected between B cells whose forces on CD40-CD40L^{K143A} bonds were limited to be <12 pN and those that allowed up to 56-pN forces (Fig. 3, E to H, and fig. S4). By comparison, we observed higher phosphorylation of these two signaling molecules when B cells were allowed to exert up to 56-pN forces on CD40-CD40L^{A208D} bonds than when the endogenous forces were limited to be <12 pN (Fig. 3, E to H, and fig. S4, A to D). Together, these results indicate that endogenous forces on CD40-CD40L bonds are necessary for B cell spreading and differentially enhance CD40 proximal signaling. X-HIgM mutations abolish spreading and diminish signaling due to their inability to form long-lived bonds at higher forces.

External force on CD40-CD40L bonds amplifies CD40 signaling

Our finding that limiting endogenous forces on CD40 suppresses B cell spreading and signaling prompted us to ask whether applying an external force to CD40 would enhance B cell signaling and function. After all, B cells exert endogenous force on CD40 and a reaction force of equal magnitude but opposite direction would be acted back to B cells through CD40 by virtue of Newton's third law. To answer this question in a high-throughput fashion, we developed a parallel magnetic force activation (PMFA) assay (Fig. 4A and fig. S5, A to D), modified from a published system (*69*). Our multi-well plate-based assay takes advantage of a 3D-printed plate lid (fig. S5A) that can house two magnets placed in the antiparallel configuration above each well, which can apply magnetic force on paramagnetic beads bearing CD40L bound to CD40 on B cells underneath the magnets (fig. S5B). While accounting for the size constraint of cell medium in each well, each magnet pair is placed as low as possible inside the wells, allowing 20-pN average force per bead ($\langle F_M \rangle$) and a peak force of ~25 pN at the center of the well (fig. S5C). To constrain the bead-bounded cells to the well center where the desired range of magnetic forces is focused, we seeded cells and beads on a poly-L-lysine (PLL)–coated 5-mm-diameter coverslip placed in the center of each well (Fig. 4A and fig. S5D). Cells seeded on the coverslip naturally concentrated toward its center, with a distribution closely matching the distribution of the magnetic force exerted on beads (fig. S5D), thus allowing force to be evenly distributed on as many cells as possible. Assuming the applied force on each bead to be shared evenly by all CD40-CD40L bonds present, we adjusted the CD40L site density coated on beads to achieve the desired steady-state average number of bonds ($\langle n \rangle$) per bead, based on the CD40 expression on B cells and the 2D affinity measured by BFP (Fig. 1H), to control the average force per bond ($f_M = \langle F_M \rangle / \langle n \rangle$) to match the endogenous force range (~10 to 20 pN) (fig. S5, E and F).

Enabled by the PMFA technological platform, we stimulated large numbers of B cells in parallel in the presence or absence of exogenous force on CD40-CD40L bonds, harvested them at various time points, stained them with fluorescence antibodies against phosphorylated p38 and Erk1/2, and analyzed them by flow cytometry (Fig. 4A). Phosphorylation of p38 and Erk1/2 in either PBMC or Farage B cells stimulated by soluble and bead-coated CD40L in plates without magnets on their lids were statistically indistinguishable, which were barely higher than those in unstimulated cells (negative control) but much lower than those in cells stimulated by anysomycin (AM) or tetradecanoylphorbol acetate (TPA) (positive control) for p38 and Erk1/2, respectively (Fig. 4, B and C). Mounting magnets on the plate lids greatly right-shifted the fluorescence histograms, indicating that applied force on CD40 up-regulated p38 and Erk1/2 phosphorylation in both PBMC or Farage B cells (Fig. 4, B and C). Compared to the results obtained in the TGT experiment by removal of the 12-pN cap to allow up to 56-pN endogenous forces on CD40 (Fig. 3, E and F), applying 10- to 20-pN exogenous forces accelerated and sustained the phosphorylation kinetics of p38 and Erk1/2, which peaked at 1 hour after stimulation and were maintained up to at least four more hours (Fig. 4, D to G).

Again, the X-HIgM CD40L mutants showed defects in force-induced p38 and Erk1/2 phosphorylation, with greater deficiencies for CD40L^{K143A} than CD40L^{A208D}, indicating that eliminating catch bonds is more defective than suppressing catch bonds (Fig. 4, B to E). The force-dependent enhancement of signaling for CD40L^{WT} and its reduction by X-HIgM CD40L mutants could be revealed by comparing the mean phosphorylation fold change of cells with and without force to the significance level (*P* value) at each time point (Fig. 4, F and G). Similarly, trends equivalent to those described above for PBMC B cells were also observed for Farage cells (fig. S5G), indicating that these results are not affected by B cell types. Moreover, as expected, all soluble CD40L constructs tested showed statistically indistinguishable results compared to those tested under no-force conditions (fig. S5, H and I). Only CD40L^{WT} showed significant force enhancement, as all but the 0 time point WT data appear in the $P < 0.05$ region (white), whereas data for both X-HIgM mutants appear in the $P > 0.05$ region (gray), consistent with their shorter bond lifetimes (Fig. 1, I and J), less endogenous force on CD40 (Fig. 2, D to I), and inability to support spreading and signaling even when endogenous forces up to 56 pN were permitted (Fig. 3, E to H). Together, these observations demonstrate how the force on CD40-CD40L bonds can enhance CD40 signaling and how X-HIgM mutations impair this force-induced signaling enhancement, regardless of B cell types and the source of the force.

Force on CD40-CD40L bonds amplifies BCR-dependent translocation of TFEB

BCR-antigen ligation in the absence of costimulation by T cells induces B cell death by apoptosis, but the underlying mechanism remained mysterious (*2*). Recently, the BCR-induced nuclear translocation of the cytosolic transcription factor EB (TFEB) was identified as a key process that governs apoptosis of B cells (Fig. 5A) (*70*). Nuclear TFEB drives B cell apoptosis through the expression of pro-apoptotic Bcl-2 family members (*70*). At the same time, TFEB is involved in rescuing B cells from apoptosis via the transcriptional up-regulation of receptors that are involved in receiving secondary salvage signals (e.g., cytokine receptors, homing receptors, and MHC-II). CD40 ligation interferes with these signal circuits in two

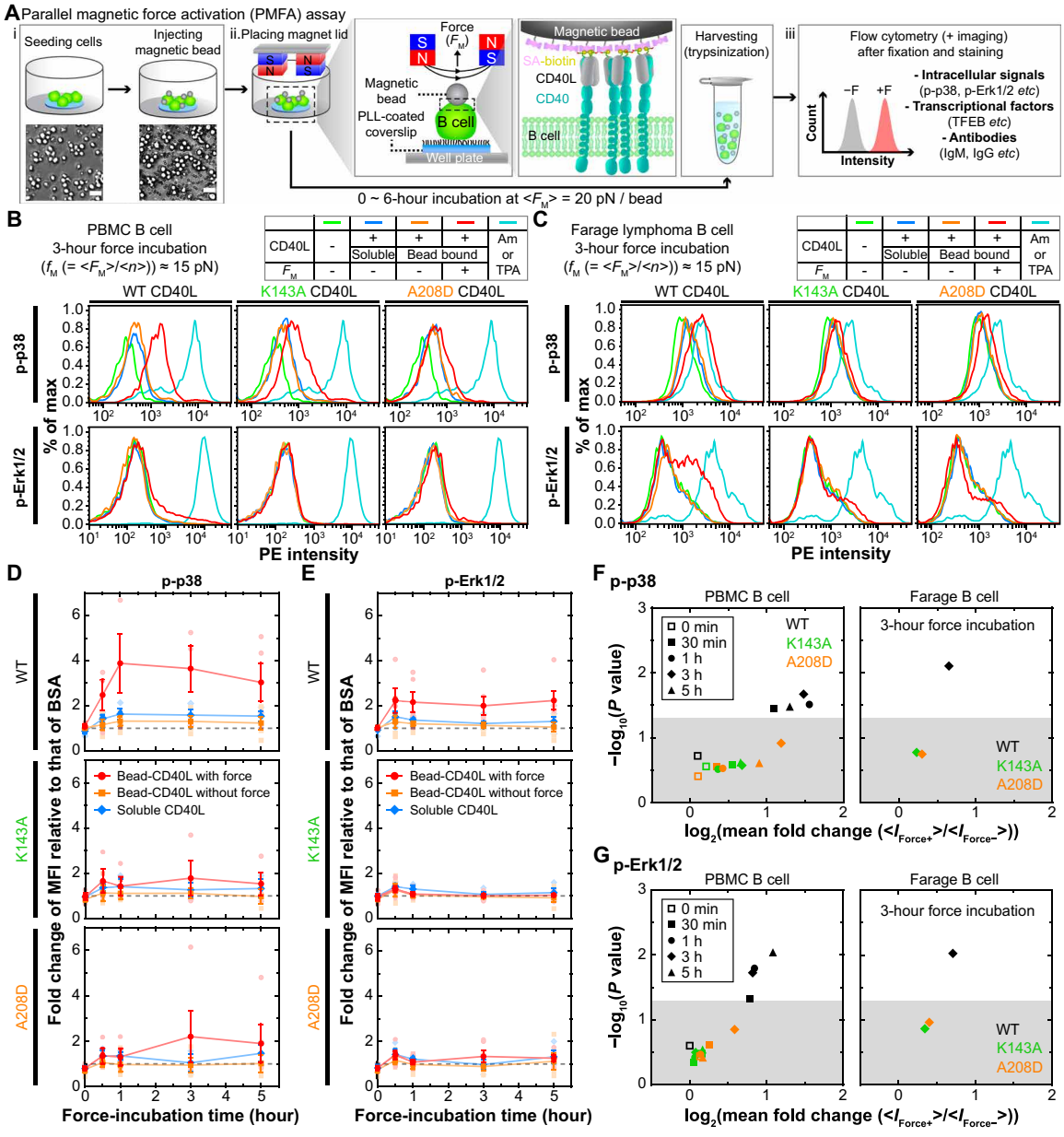

Fig. 4. Exogenous forces on CD40-CD40L bonds amplify CD40 signaling, and X-HIgM mutations abrogate this amplification. (**A**) Schematic of the PMFA assay. (i) Diagram (top) and representative images (bottom) of B cells placed on PLL-coated circular coverslip (5 mm diameter) at the well center (left) onto which magnetic beads (2.8 μm diameter) functionalized with CD40L are added (right). Scale bar, 40 μm. (ii) Zoom-out (first left) and zoom-in (second left) views showing how an average force of $\langle F_M \rangle$ ~ 20 pN/bead is applied on beads by placing an antiparallel pair of 5-mm cubic neodymium magnets above each well. This force is supported by the CD40-CD40L bonds (second right). After 0 to 6 hours of incubation, cells are harvested (first right). (iii) Cells are analyzed by flow cytometry. (**B** and **C**) Keys (tables) and representative histograms of fluorescence staining of p-p38 (top row) and p-Erk1/2 (bottom row) of PBMC (B) and Farage (C) B cells stimulated by soluble or bead-bound CD40L constructs without or with 3-hour force application. Negative (no stimulation) and positive (AM or TPA stimulation) controls are also shown. (**D** and **E**) Mean ± SEM and individual points ($N \geq 3$ with $n > 10{,}000$ cells) of fold change of MFI relative to that of BSA for p-p38 (D) and p-Erk1/2 (E) in PBMC B cells stimulated by soluble (blue) or bead-coated CD40L constructs with (red) or without (orange) force are plotted versus incubation time. (**F** and **G**) Log plots of P value (assessed by two-sided t test) versus mean fold change of MFI of p-p38 (F) and p-Erk1/2 (G) in PBMC (left) and Farage (right) B cells between stimulations by bead-bound CD40L without and with force. Different scatter points represent different time points, and different colors indicate different CD40L constructs. Shaded area represents $P > 0.05$ above which indicates region of statistical significance.

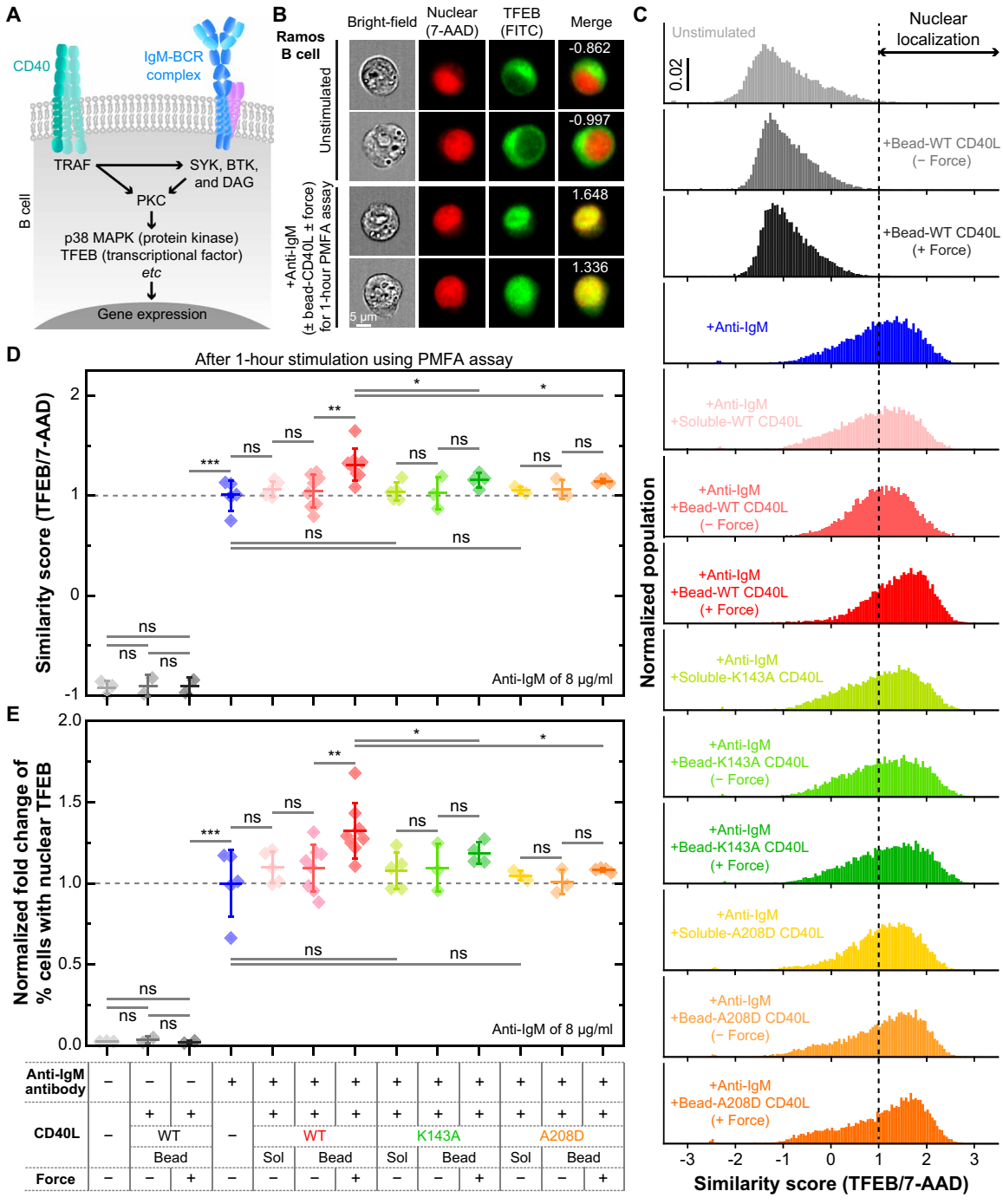

Fig. 5. Force on CD40-CD40L bonds amplifies BCR-induced translocation of TFEB, and X-HIgM mutations abrogate this amplification. (**A**) Brief summary of B cell signaling downstream of CD40 and BCR. (**B**) Representative bright-field (first column) and fluorescence (second to fourth columns) images of Ramos B cells from image flow cytometer without (first two rows) and with (last two rows) PMFA-exerted force on CD40-CD40L bonds. Nucleus and transcription factor EB (TFEB) are stained by 7-AAD (second column) and FITC (third column), respectively. The yellow color in the merged image (fourth column), resulting from overlapping of the red and green fluorescence, reveals the translocation of TFEB into the nucleus, as quantified by the similarity scores (see Materials and Methods). (**C**) Normalized populations of similarity scores for different conditions as indicated by different colors in the different panels (in descending order): unstimulated (light gray), bead-coated CD40L^{WT} without force (dark gray), soluble anti-IgM antibody (blue), soluble anti-IgM plus soluble CD40L^{WT} (pink), soluble anti-IgM plus bead-coated CD40L^{WT} without force (light red), soluble anti-IgM plus bead-coated CD40L^{WT} with force (dark red), soluble anti-IgM plus soluble CD40L^{K143A} (light green), soluble anti-IgM plus bead-coated CD40L^{K143A} without force (green), soluble anti-IgM plus bead-coated CD40L^{K143A} with force (dark green), soluble anti-IgM plus soluble CD40L^{A208D} (yellow), soluble anti-IgM plus bead-coated CD40L^{A208D} without force (light orange), and soluble anti-IgM plus bead-coated CD40L^{A208D} with force (orange). (**D** and **E**) Mean ± SD with individual data points ($N \geq 3$ with $n > 10{,}000$ cells) of fold change of similarity score (D) and % cells with nuclear TFEB normalized by anti-IgM only data (E). Different colors indicate different conditions [matched with those in (C)]. Statistical significance in differences among conditions was assessed by two-sided *t* test.

ways. On the one hand, CD40 activation antagonizes the TFEB-induced expression of proapoptotic Bcl-2 family members by triggering the expression of the anti-apoptotic family member Bcl-xL, which consequently halts the apoptotic process. On the other hand, CD40 signaling sustains the nuclear residency of TFEB, thereby further promoting the expression of TFEB-controlled salvage elements and concomitant B cell survival (*70*).

Since force on CD40 affected bond kinetics and signaling, we hypothesized that force on CD40-CD40L bonds would promote CD40-induced TFEB translocation. To test this hypothesis, we combined our PMFA assay with imaging flow cytometry to measure the localization of TFEB following BCR stimulation with soluble anti-IgM and CD40 stimulation with magnetic bead–bound CD40L in the presence or absence of magnets using a similarity score to quantify the overlap between the TFEB [fluorescein isothiocyanate (FITC)] and the nucleus [7-amino-actinomycin D (7-AAD)] staining (Fig. 5B). Because of the lack of BCR expression on Farage cells, we switched to Ramos B cells after confirming that their force-dependent interaction kinetics of CD40 with CD40L and its X-HIgM mutants were similar to Farage and PBMC B cells (fig. S6, A to C). Consistent with a previous study (*70*), Ramos cells stimulated with soluble anti-IgM had markedly increased translocation of TFEB with a higher portion of cells with nuclear TFEB as indicated by the higher similarity score, compared to cells without BCR stimulation whose TFEB was mostly localized in the cytoplasm with a low similarity score (Fig. 5, B to E, and fig. S6, D to F). We next compared the effect of costimulation by soluble or bead-bound CD40L in the absence and presence of exogenous force on the BCR-stimulated TFEB translocation by normalizing the similarity score and proportion of cells with nuclear TFEB to that of B cells stimulated with soluble anti-IgM alone (Fig. 5, D and E). Remarkably, while both soluble and bead-bound CD40L showed statistically indistinguishable TFEB translocation in the absence of force, applying force to CD40-CD40L bonds significantly increased the similarity score and the portion of cells with nuclear TFEB (Fig. 5, D and E). In sharp contrast, X-HIgM CD40L mutants showed no force-induced increase in TFEB translocation when compared to BCR stimulation alone. These findings indicate that force on CD40 is required for the additional enhancement of TFEB translocation costimulated by soluble anti-IgM and bead-coated CD40L (relative to soluble anti-IgM stimulation alone), and that X-HIgM CD40L mutants do not support such additional enhancement.

Force on CD40-CD40L bonds promotes antibody class switch and allows discrimination between WT CD40L and X-HIgM mutants

To put our hypothesis that mechanotransduction governs CD40 function and dys-mechanoregulation underlies X-HIgM to a final test, we examined whether, and if so, how force may affect long-term B cell function during GC formation, B cell differentiation, and CSR. This is especially important in light of the observed defects in X-HIgM CD40L mutants' ability to support CD40 mechanotransduction, which correlates with their known defects in CSR leading to X-HIgM pathology. To study the effect of force on such B cell functions, we mimicked the GC reaction by an in vitro assay that allows us to induce CD40L-dependent B cell activation, differentiation, and CSR by coculturing PBMC B cells with CD40L-coated beads in the presence of IL-4, IL-21, and BAFF (*71*–*73*), and combining this with or without force application on CD40-CD40L bonds by the PMFA technique (Fig. 6A and fig. S7, A and B). After force application for the initial 6 hours followed by prolonged coculture for 8 days, B cell phenotypes and Ig types were measured by flow cytometry (fig. S7, A and B) with appropriate fluorescence minus one (FMO) controls (*71*). Using this setup, no significant changes in the total $CD19^+$ population, $CD19^+CD27^+CD38^+$ activated B cell–like fraction, or $CD19^+CD27^+CD38^-$ memory-like B cell (MBC) fraction of B cells were observed when comparing WT CD40L to X-HIgM CD40L mutants in the presence or absence of force (Fig. 6, B and C, and fig. S7, C and D). These markers were used based on recent reports of in vitro human B cell cultures (*71*). For the entire $CD19^+$ B cell populations, the IgM^+ portions were similar across all CD40L constructs with or without force (Fig. 6D and fig. S7E, IgM^+ in entire $CD19^+$). By comparison, the IgG^+ portion was significantly higher for $CD40L^{WT}$, and significantly lower for X-HIgM CD40L mutants, in the presence compared to in the absence of force, despite that without force CD40L induced lower IgG^+ portion than its X-HIgM mutants (Fig. 6D and fig. S7E, IgG^+ in entire $CD19^+$).

To obtain further support to the above results, we analyzed the IgM^+ portions in the MBC and activated B cell–like subsets, finding no differences among CD40L constructs in the absence of force (Fig. 6D and fig. S7E, IgM^+ of MBC and $CD19^+CD27^+CD38^+$ activated B cell), akin to the result obtained from analyzing the overall B cell population (Fig. 6D, IgM^+ in entire $CD19^+$). Similar to the overall B cell population, in the presence of force, the IgG^+ portion of activated B cell–like subsets was significantly increased by $CD40L^{WT}$ and significantly decreased by X-HIgM CD40L mutants (Fig. 6D, IgG^+ in activated B cell–like subsets). The IgG^+ portion of MBC followed similar but less pronounced trends (Fig. 6D and fig. S7E, IgG^+ in MBC $CD19^+$). The data in Fig. 6D obtained using PBMCs from a representative donor were confirmed by repeated experiments using two other donors (Fig. 6E and fig. S7, F and G). The data not only show that force up-regulates CSR induced by $CD40L^{WT}$ and down-regulates CSR induced by X-HIgM CD40L mutants but also suggest that force enables CD40 to distinguish between $CD40L^{WT}$ and its X-HIgM mutants in terms of their ability to induce CSR, recapitulating the pathology of X-HIgM. The inability of CD40 to discriminate between $CD40L^{WT}$ and X-HIgM CD40L mutants in the absence of force demonstrates that force on CD40 leads to enhanced CSR and is required to reproduce the detrimental effects of the CD40L mutations on CSR as observed in X-HIgM patients, shedding light on the disease mechanism.

Effective 2D affinity or bond lifetime at optimal force predicts B cell signaling outcome and functions

After obtaining six sets of data using four mechanobiological techniques, we asked the question of whether there are and, if so, what may be the underlying causative relationships among these data. Whereas the connection from B cell signaling (e.g., phosphorylation of p38 and Erk1/2 as well as TFEB translocation) to function (e.g., CSR) may be intuitively conceivable, their link to CD40-CD40L binding parameters seems less apparent. Our work first extended the binding parameters from the 3D ones measured in the fluid phase to their 2D counterparts measured in situ at the B cell membrane, including the apparent effective zero-force 2D on-rate $A_c k_{on,0}$, the apparent zero-force off-rate $k_{off,0}$, and their ratio, the apparent effective 2D affinity at zero-force $A_c K_{a,0} = A_c k_{on,0}/k_{off,0}$ (Fig. 1, D to H, and fig. S1, D and E) (*35*, *37*, *74*). Since the data in Figs. 2 to 6 and figs. S2 to S7 suggest the importance of force, we also examined the force-dependent bond lifetime $\langle t_b \rangle(f)$. This is a natural extension of the zero-force

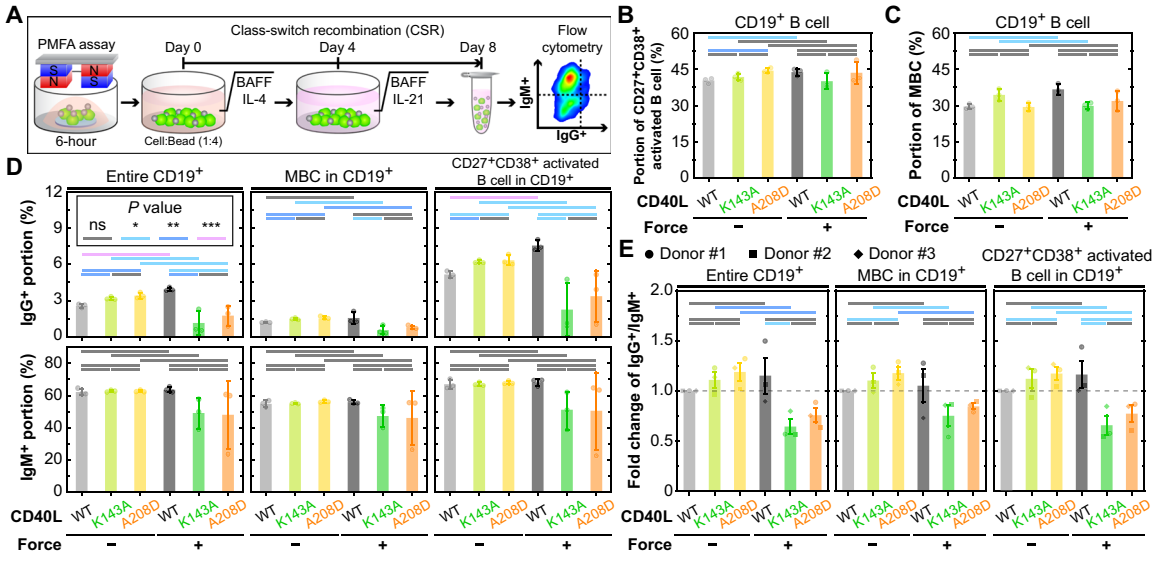

Fig. 6. Force on CD40-CD40L bonds promotes antibody class switch for WT CD40L and impairs class switch for X-HIgM mutants. (**A**) Schematic of procedure and working principle for measuring class-switch recombination with the PMFA assay. After 6 hours of force application, cells are incubated with cytokines for 8 days (soluble BAFF and IL-4 for the first 4 days and soluble BAFF and IL-21 for the last 4 days). On day 8, cells are harvested, fixed, permeabilized, and stained to measure antibodies expressed on the membrane by flow cytometry. (**B**) Mean ± SD with individual data ($N = 3$ with $n > 10{,}000$ cells) of $CD19^+CD27^+CD38^+$ activated B cell subpopulation among the entire population of $CD19^+$ B cells from a representative donor stimulated by the indicated bead-bound CD40L constructs with and without force. (**C**) Mean ± SD with individual data ($N = 3$ with $n > 10{,}000$ cells) of $CD19^+$ memory B cell (MBC) subpopulation among the entire population of $CD19^+$ B cells from a representative donor stimulated by the indicated bead-bound CD40L constructs with and without force. (**D**) Mean ± SD with individual data points of IgG^+ (top row) and IgM^+ (bottom row) portions in all $CD19^+$ B cells (first column), MBC (second column), and $CD19^+CD27^+CD38^+$ activated B cells (third column) from a representative donor stimulated by the indicated bead-bound CD40L constructs with and without force. (**E**) Mean ± SEM ($N = 3$) of force-stimulated fold change of IgG^+ to IgM^+ ratio normalized by the $CD40L^{WT}$ stimulation without force in all $CD19^+$ B cells (left), MBC (middle), and $CD19^+CD27^+CD38^+$ activated B cells (right) from three donors stimulated by the indicated bead-bound CD40L constructs with and without force. Statistical significance in differences among groups was assessed by two-sided *t* test.

reciprocal off-rate $1/k_{off,0}$ (see fig. S1F) by including the force modulation of bond dissociation. To include the apparent effective 2D on-rate $A_c k_{on,0}$ that is also affected by the X-HIgM mutations, we also extended the zero-force apparent effective 2D affinity from a value to a curve by replacing $1/k_{off,0}$ by $\langle t_b \rangle(f)$ in the affinity definition to define a "force-dependent apparent effective 2D affinity" $A_c K_a(f) = A_c k_{on,0} \times \langle t_b \rangle(f)$ (Fig. 7A) (*35*, *37*, *74*, *75*). It is evident from the $A_c K_a$ ratio versus f curves that force amplifies the difference in this affinity-like parameter characterizing the binding propensity of CD40 with CD40L between WT and mutants until reaching ~15 pN, the optimal force where the lifetime of the CD40-$CD40L^{WT}$ catch-slip bond peaks (Fig. 7B). This is similar to the observation that catch bond amplifies TCR discrimination of agonist versus antagonists (*45*, *76*).

After extensive correlative analyses, we found that, among all binding parameters tested, $A_c K_a$(15 pN) and $\langle t_b \rangle$(15 pN), two force-dependent binding parameters evaluated at the optimal force, where the CD40-$CD40L^{WT}$ catch bond transitions to the slip bond, stand out as the best correlators for CD40-mediated B cell signaling and function (Fig. 7, C and D, and fig. S8). This can be clearly seen from the Pearson's r correlation maps showing much better correlations of $A_c K_a$(15 pN) and $\langle t_b \rangle$(15 pN) than $A_c K_{a,0}$ and $1/k_{off,0}$ with all the results of the MTP, TGT, and PMFA experiments (Fig. 7E), highlighting a key role of force in regulating function through modulating binding.

DISCUSSION

Ligand binding and signaling of CD40 are critical elements for the communication between B and T cells, and hence orchestrate antibody-mediated immune responses (*77*). Effective T-B communication in GC ensures the production of high-affinity, class-switched antibodies to provide appropriate and long-lasting immunity against pathogens. Dysregulation of ligand binding and/or signaling of CD40 causes immunodeficiencies, such as the X-HIgM, characterized by abnormal antibody isotype production and increased susceptibility to opportunistic infections. Surprisingly and unlike other types of immunoreceptors, nothing is known about CD40-mediated mechanobiology and whether mechanotransduction plays a role in X-HIgM. Here, we identified CD40 as a bona fide mechanoreceptor and mechanosensor by uncovering the crucial role of mechanotransduction in regulating CD40 signaling output, which subsequently affects B cell function. We also showed that X-HIgM–associated variants of CD40L, as well as variants obtained from published mutagenesis studies (*24*, *38*–*42*), were unable to induce proper CD40 mechanotransduction, which is likely to contribute to the antibody deficiency syndromes in affected patients. These results were achieved by using a suite of biomechanical techniques, including some that were newly developed here, which were integrated with more conventional immunological techniques to comprehensively examine various aspects of the mechanotransduction of a single immunoreceptor.

Using a BFP to mechanically analyze CD40-CD40L interaction kinetics at the single-bond level in situ, we found that pathogenic X-HIgM CD40L variants display reduced zero-force apparent effective 2D affinities for CD40 compared to $CD40L^{WT}$. Such 2D measurements more closely resemble interactions at the cell membrane compared to 3D measurements using soluble proteins separated from the cellular environment, such as by the surface plasmon resonance

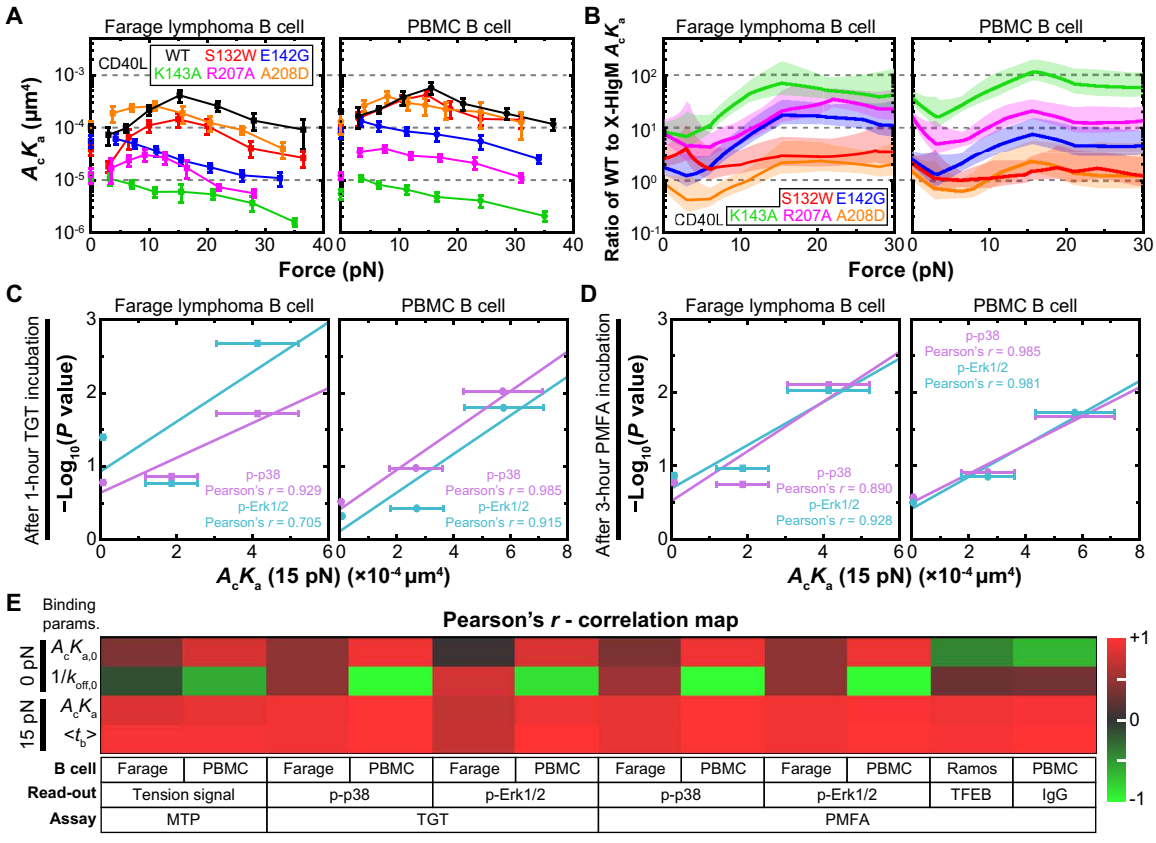

Fig. 7. Effective 2D affinity and bond lifetime at optimal force predict B cell signaling and functions. (**A**) Force-dependent 2D affinity-like parameters [$A_cK_a(f) = A_ck_{on,0} \times \langle t_b \rangle(f)$, calculated using $A_ck_{on,0}$ from Fig. 1H and fig. S1E, and $\langle t_b \rangle(f)$ from Fig. 1, I and J] (*75*) of CD40 for the indicated CD40L constructs at the membrane of Farage and PBMC B cells versus force *f*. (**B**) Ratios of $A_cK_a(f)$ of WT CD40L to those of X-HIgM CD40L mutants versus force *f*, showing how force amplifies the differential affinities between WT and X-HIgM CD40Ls in Farage and PBMC B cells. (**C** and **D**) Semi-log correlation plots of A_cK_a(15 pN) of CD40 interaction with CD40L constructs, with the *P* values (from Figs. 3, G and H, and 4, F and G) quantifying statistical significance in signaling differences (p38 and Erk1/2 phosphorylation) between groups in Farage or PBMC B cells stimulated by the same CD40L constructs under force at two time points in TGT (C) and PMFA (D) experiments. Data are presented as mean ± SEM [calculated using the Gaussian error propagation law for A_cK_a(15 pN), $n = 3$ to 4 bead-cell pairs for $A_ck_{on,0}$ and ~35 measurements for $\langle t_b \rangle$(15 pN)] and linearly fit for each group of three points generated using $CD40L^{WT}$, $CD40L^{A208D}$, and $CD40L^{K143A}$ with the degree of correlation quantified by Pearson's *r* coefficient. (**E**) Correlation maps [assessed by Pearson's *r* coefficient for all readouts (C), (D), and fig. S8] showing how CD40 signaling and downstream functions measured from the indicated experiments correlate poorly with 2D affinity ($A_cK_{a,0}$) and reciprocal off-rate ($1/k_{off,0}$) measured in the absence of force (0 pN, top half), yet correlate strongly with the same binding parameters [A_cK_a(15 pN), $\langle t_b \rangle$(15 pN)] when measured at the optimal force (15 pN, bottom half); from left to right: MTP, phosphorylation of p38 and Erk1/2 by TGT, and phosphorylation of p38 and Erk1/2, TFEB translocation, and Ig class switch by PMFA.

technique. Reasons include the fact that the in vivo CD40-CD40L interaction takes place the surfaces of a B cell and a T cell in direct physical contact so that our assays enable us to recapitulate not only protein-intrinsic properties local to the CD40-CD40L binding domains but also CD40 membrane organization, diffusion, and possibly other factors on the B cell plasma membrane, which are completely absent in 3D measurements. A caveat here is the use of the simplest kinetics model to evaluate $A_cK_{a,0}$, which assumes binding to occur as a second-order forward, first-order reverse, single-step bimolecular interactions between a CD40 monomer and a CD40L monomer. The real CD40-CD40L interaction likely involves multivalent interaction (*41*), which would require a more sophisticated model for its description. In the present paper, we treat $A_cK_{a,0}$ as an apparent effective 2D affinity to compare relative binding propensities of CD40 coated on beads or expressed on PBMC and Farage B cells interacting with $CD40L^{WT}$ or five CD40L mutants. Future studies will test different multivalent binding kinetics mechanisms to determine the most appropriate one for the CD40-CD40L interaction and replace the apparent kinetic and affinity parameters by the intrinsic parameters.

Analysis of bond dissociation under force showed that CD40 forms a catch-slip bond with $CD40L^{WT}$, which is quite interesting in its own right. More strikingly, X-HIgM CD40L mutants suppress or even eliminate the catch bond (Fig. 1, I and J, and fig. S1), revealing additional defects of the X-HIgM CD40L mutants in the presence of force. The utility and usefulness of these measurements were further demonstrated by their power in predicting B cell signaling and function (Fig. 7, C to E, and fig. S8). Another caveat here is that multivalent interaction may also give rise to the appearance of a catch bond (*78*). In the present paper, we use the measured bond lifetime versus force curves to compare how force modulates the dissociation of CD40 coated on beads or expressed on PBMC and Farage B cells from $CD40L^{WT}$ or five CD40L mutants. Future studies will test different kinetics mechanisms for dissociation of multivalent bonds to determine the most appropriate one for the

CD40-CD40L interaction and express the measured bond lifetime versus force curves in terms of intrinsic parameters.

The observation that X-HIgM CD40L mutants manifest more defects in the presence than in the absence of force prompted us to obtain direct evidence that CD40-CD40L bonds experience force. Not only have we obtained such evidence but our data also suggest that B (and T) cells sample their mechanical environment by generating force to pull on immobilized CD40L (and CD40), which are by themselves interesting and give context to the force-dependent CD40-CD40L bond lifetime measurements. More intriguingly, B cells seem to be able to fine-tune their endogenous force to match the level sustainable by the CD40-CD40L anchor, as demonstrated by three lines of evidence (Fig. 2 and fig. S2). First, the forces B cells exerted on $CD40L^{WT}$ were between 12 and 19 pN, closely matching the optimal force where the lifetime of the CD40-$CD40L^{WT}$ bond peaks as it transitions from the catch to slip regime. Second, when CD40 was bound to the MTP surface by an anti-CD40 antibody, the number of CD40 experiencing above-threshold force decreased steeply as the threshold increased, matching the slip-only bond profile of the CD40–anti-CD40 bonds, suggesting that the endogenous force follows the ability of the CD40 anchor to sustain force even when the latter changes. Third, when CD40 interacted with the MTP-tagged X-HIgM CD40L mutants, B cells were much less able to exert above threshold forces on these bonds, again matching their respective suppressed catch-slip bond and the slip-only bond profiles. We should note that how the MTP force readout depends on the binding parameters remains somewhat elusive. To generate a force signal, CD40 must form durable bonds with MTP-tagged surface-bound CD40L or anti-CD40 antibody capable of sustaining force, hence depending on the force-dependent binding kinetics. However, this alone is insufficient because beads coated with soluble CD40 can bind CD40L with the same binding parameters as B cell surface CD40 but placing such beads on MTP surface would not generate any force signal. Therefore, extracellular ligand binding must induce intracellular signaling to activate the force generation and transmission machinery to result in an MTP readout, suggesting an interplay between binding kinetics and endogenous force generation to allow B cells to mechanically sample CD40L, and implying that mechanotransduction underlies T-B cell communication. By using pharmacological agents to inhibit actin polymerization, Rock, and myosin IIA, we found that the actin-myosin cytoskeleton is required for the B cell to generate and exert force on CD40. Still, which adaptor, scaffold, and signaling molecules mediate and regulate this active process remains an open question for future research. We suggest three possible force transmission pathways: (i) tension through scaffolding proteins connecting intracellular domain of CD40 and reorganized actin cytoskeleton [e.g., via TNFR-associated factor (TRAF)], (ii) membrane-linked tension arisen from CD40 oligomerization and recruitment of adaptors, and (iii) indirectly transmitted tension by adhesion molecules. Additionally, since CD40L forms a structurally undefined higher-order oligomer that remains soluble and functional, particularly when scaffolded with surfactant proteins (*79*, *80*), it may also be intriguing future research to investigate whether binding of soluble CD40L multimers induces forces in monomeric members of CD40 clusters on B cells; if so, how, and if not, how such binding triggers signaling.

The reasoning that MTP readout reports cell signaling prompted us to further examine the effect of limiting the endogenous force experienced by a CD40-CD40L bond below a threshold. We used TGT to examine how limiting force affected cell spreading as previously done by others (*51*, *57*, *81*). More innovatively, we extended the previous coverslip-based technique (Fig. 3A) to a bead-based method (Fig. 3D) amenable to the analysis of intracellular signaling, which enabled us to find that endogenous forces are required for proper B cell spreading on CD40L and enhance CD40 signaling (Fig. 3 and fig. S4). When the endogenous forces exerted on CD40-CD40L bonds were confined to <12 pN, B cells could not efficiently spread on CD40L, which was accompanied by reduced phosphorylation of key signaling molecules, compared to circumstances where bonds were allowed to experience forces up to 56 pN. In contrast to $CD40L^{WT}$, X-HIgM mutants failed to support appreciable spreading and abrogated signaling regardless of whether forces were restricted to <12 pN or allowed to be increased up to 56 pN (Fig. 3 and fig. S4), confirming the pivotal role of mechanotransduction in CD40 triggering and providing an explanation for the pathological behavior of X-HIgM variants in terms of dysregulated mechanotransduction. Similar to MTP, how the TGT force readout depends on the binding kinetics is not fully understood. Different from MTP, which reports the number of CD40-CD40L bonds on which an above threshold force is applied by the B cell, TGT reports the force requirement on CD40-CD40L bonds for function. Together, these two techniques provide different yet complementary perspectives of B cell endogenous forces induced by and exerted on CD40-CD40L bonds and the functional consequences of preventing B cell from exerting such forces.

We then turned the table around to examine the effects of exogenous instead of endogenous forces, because of the technical innovation of the PMFA technique. Three types of CD40-mediated B cell functions were quantified: intracellular signaling (short-term), TFEB translocation (mid-term), and CSR (long-term). Compared to the TGT experiment finding that limiting endogenous force decreases signaling (Fig. 3, E to H), the PMFA experiment found that exerting exogenous force increases signaling (Fig. 4, D to G), showing two sides of the same coin. X-HIgM mutants, instead, are defective in their ability to induce force-dependent enhancement of CD40 signaling (Fig. 4, D to G, and fig. S5, G to I), also consistent with the MTP results (Fig. 2, H and I, and fig. S2). Analogously to proximal CD40 signaling, mechanotransduction of externally applied force on CD40-CD40L bonds induced prolonged nuclear localization of TFEB, necessary for the induction of secondary signals to rescue B cells from BCR-induced apoptosis, while X-HIgM mutations to CD40L abrogate this prolonged nuclear localization of TFEB (Fig. 5, D and E, and fig. S6). Enabled by our PMFA in vitro CSR assay, we demonstrated that force on CD40-CD40L bonds promotes CSR in activated and memory-like B cells as well as B cells as a whole. While in the absence of force X-HIgM CD40L mutants showed no difference in their ability to induce CSR compared to $CD40L^{WT}$, in the presence of force these mutants down-regulated CSR (Fig. 6, B to E, and fig. S7). Mechanotransduction, rather than affinity, is responsible for these observations. This is clearly demonstrated by $CD40L^{A208D}$, a mutation found in X-HIgM patients, as its affinity for CD40 at zero force is equivalent to that of $CD40L^{WT}$, and yet this mutation abrogates CSR, correlating the disease to the inability of $CD40L^{A208D}$ to form catch bonds, rather than its zero-force affinity. Thus, CD40 mechanotransduction enables B cells to distinguish between $CD40L^{WT}$ and its X-HIgM variants in terms of their ability to induce Ig class-switch recombination as CD40 could not discriminate between them without applied force. In other words,

for the CD40L mutations to manifest defects in X-HIgM, their participation in CSR must involve CD40 mechanotransduction.

The remarkable ability of CD40-CD40L interaction kinetics to be modulated by force, manifesting as catch-slip bond formation demonstrated in this study, adds to a growing list of immunoreceptor-ligand interactions that have been observed to form catch-slip bonds, highlighting the importance of mechanotransduction through immunoreceptors (*32*). In contrast to integrins whose catch bonds are mostly linked to their adhesive functions (*82*–*89*), here we show that the CD40-CD40L catch bond affects signaling and immunological function such as CSR. Previously, the connections of TCR (*45*), pre-TCR (*90*), chimeric antigen receptor (*91*), Fcγ receptor IIA (*92*), and NKG2D's (*93*) catch bonds to signaling and function of T cells, neutrophils, and natural killer cells have been established by applying external forces to these receptor-ligand bonds while observing intracellular calcium fluxes concurrently (*45*, *94*) and by correlating altered catch bonds and functions via mutations in the receptors and/or ligands (*45*, *90*–*98*). Here, by comparison, the immunological relevance of the CD40-CD40L catch-slip bond and its role in mechanotransduction have been more directly and thoroughly demonstrated. We used four approaches to obtain multiple lines of convincing evidence: (i) matching the optimal force of the catch-slip bond to the optimal force that B cells generate, (ii) suppressing B cell signaling by capping endogenous forces below the optimal level, (iii) applying external forces to CD40-CD40L bonds while monitoring B cell signaling and function concurrently, and (iv) correlating altered catch bonds, signaling, and function via CD40L mutations found in X-HIgM patients (Fig. 7 and fig. S8). This would not have been possible without the technical innovation in the TGT and PMFA assays and without the organic integration of the four powerful mechanobiological techniques discussed earlier, serving as a roadmap to study mechanotransduction in the receptor-mediated communication between immune cells in health and disease.

We should note that CD40-CD40L bond lifetimes were measured by the BFP force-clamp assay where the force was kept constant with zero loading rate. Also, in the PMFA experiment, constant magnetic force was applied to the CD40-CD40L bonds. By comparison, a recent paper reported the first measurement of physiological loading rates cells apply to integrins, which range from 0.5 to 4 pN/s and were about three times higher in leukocytes than in epithelial cells (*99*). Also, force levels of MTP and TGT were calibrated under conditions possibly different from those that B cells exerted on CD40-CD40L bonds and from those used in BFP and PMFA experiments. Therefore, caution must be exercised when comparing the force values reported by the MTP experiment, limited by the TGT experiment, and applied in the BFP and PMFA experiments.

Whereas CD40 signaling is decreased by capping endogenous force and increased by applying exogenous force, differences in the effect size and timing have been observed between the TGT (Fig. 3, E to H, and fig. S4) and PMFA (Fig. 4, D to G, and fig. S5) experiments. Such differences can be reconciled by considering the size difference between the TGT beads and the PMFA beads, as well as the different CD40L densities used in the two experiments. The magnetic beads used in the PMFA are unlikely able to support endogenous force generation due to their smaller size and the lower CD40L density required to limit the number of formed bonds per bead-cell contact to be ~2. In sharp contrast, the much larger TGT beads functionalized with much higher CD40L density would allow their formation of a much greater number of bonds with B cell CD40 over a much larger contact area to induce stronger signaling, which should promote endogenous force generation. Moreover, it is possible that while endogenous forces may rise and decay after contact formation, leading to a similar rise and fall of CD40 signaling in the TGT experiment, exogenous forces were continuously applied to CD40-CD40 bonds in the PMFA experiment, favoring sustained p38 and Erk1/2 phosphorylation.

The phosphorylation of p38 and Erk1/2 is differentially enhanced by force, much greater for p38 than Erk1/2. This indicates that the p38 signaling pathway may play a greater role in CD40 mechanotransduction than the Erk1/2 signaling pathway. Differential responses to the same mechanical stimulation have been observed in other systems. For example, mechanosensing through platelet glycoprotein Ib switches integrin $\alpha_{IIb}\beta_3$ from the low-affinity state to the intermediate affinity state, but does not do so for integrins $\alpha_V\beta_3$ and $\alpha_5\beta_1$ (*89*). An interesting future study would be to elucidate the shared and distinct components in the p38 and Erk1/2 signaling pathways used by or independent of CD40 mechanotransduction.

The physiological sources of external forces applied to CD40 are of great interest. As mentioned earlier, the mechanical interaction between highly mobile T and B cells predicts that CD40-CD40L bonds are likely subjected to physical forces (*32*). In addition, due to the ability of T cells to generate endogenous force on their membrane receptors, such as TCR (*46*, *52*, *100*), program death 1 (PD-1) (*53*), and lymphocyte function–associated antigen 1 (LFA-1) (*81*), it is conceivable that T_{FH} cells could also apply endogenous force to CD40-CD40L bonds to balance the endogenous B cell force and thus promote the elevated and sustained CD40 signaling, TFEB translocation, GC reaction, and CSR. Our experiment shows that T_{FH} cells do indeed exert force on CD40L. The earlier discussion of B cell force on CD40 suggests that T cell force on CD40L should also require T cell signaling induced by CD40L upon binding to CD40. Elucidating whether and how force, be it from T or B cells, may affect CD40L signaling in T cells is an open question worthy of future exploration.

The central role of mechanotransduction in enabling CD40 activation demonstrated in this study may have far-reaching implications with respect to other category II TNFRs. Not only has it not been understood why they are unable to be activated by soluble ligands despite similar ligand binding affinity compared to category I TNFRs (*26*–*28*), but also their ability to be activated by membrane-bound ligands is also indicative of a possible role for mechanotransduction for the category II TNFRs in general. Screening of other category II TNFRs such as TNFR2, 4-1BB, Fas, OX40, CD27, and TNF-related apoptosis-inducing ligand (TRAIL) for their mechanotransduction abilities may provide a promising avenue for understanding immunological disorders associated with such receptors. Furthermore, CD40 itself is expressed on cells other than B cells, such as dendritic cells and macrophages (*101*). Helper T cells license antigen-presenting cells via CD40-CD40L interaction to activate cytotoxic T cells, providing a bridge between helper and cytotoxic T cells (*101*–*104*). Thus, future research of CD40 mechanotransduction in dendritic cells and macrophages could have broad implications in anti-cancer and anti-pathogen immunity.

To conclude, our findings establish that mechanical forces regulate the CD40-CD40L bond lifetime and shed light on the mechanistic underpinnings of X-HIgM syndrome by demonstrating that dysregulation of mechanotransduction mediated by CD40-CD40L interaction underlies the pathology observed in X-HIgM patients. This study improves our understanding of T-B

cell interactions and potentially opens new therapeutic avenues for the treatment of X-HIgM.

MATERIALS AND METHODS

Cells

To generate the protein producer cell line HEK293T/17 BirA$^+$, HEK293T/17 cells [purchased from American Type Culture Collection (ATCC)] were transduced with the plasmid pHR-CMV-TetO2_HA-BirA-ER encoding a green fluorescence protein (GFP) marker and hemagglutinin (HA)–tagged endoplasmic reticulum (ER)–resident *Escherichia coli* biotin ligase (a gift from A. R. Aricescu, Addgene plasmid #113897) to allow for in vivo biotinylation at the N terminus of CD40L ectodomain. HEK293T/17 BirA$^+$ cells were subsequently transduced with soluble CD40L-encoding lentiviruses to generate producer cell lines stably expressing each soluble CD40L construct. HEK293T/17 BirA$^+$ CD40L$^+$ cells were then sorted with their GFP marker to equalize expression. Farage B lymphoma cells were a gift from W. Béguelin (Weill Cornell Medical College) and maintained in RPMI 1640 supplemented with 10% fetal bovine serum (FBS), 1% penicillin-streptomycin, and 10 mM Hepes. Ramos cells (from J.W.'s laboratory) were maintained in RPMI 1640 supplemented with 10% FBS, 1% penicillin-streptomycin, 10 mM Hepes, 1 mM L-glutamine, 1 mM sodium pyruvate, and 50 μM β-mercaptoethanol. PBMC-derived B cells were purified from freshly isolated blood of healthy donors according to the protocol approved by the Institutional Review Board (IRB) of the Georgia Institute of Technology. Briefly, whole lymphocytes were separated by centrifugation with Histopaque-1077 (Millipore Sigma) from which CD19$^+$ B cells were purified using EasySep Human CD19 Positive Selection Kit II (STEMCELL Technologies). After purification, PBMC B cells were kept in RPMI supplemented with 10% FBS, 1% penicillin-streptomycin, 10 mM Hepes, and 1× nonessential amino acids, and used immediately for each experiment.

Jurkat E6.1 T cells (purchased from ATCC) were maintained in RPMI 1640 supplemented with 10% FBS, 1% penicillin-streptomycin, 10 mM Hepes, and 1 mM sodium pyruvate. To induce CD40L expression, Jurkat T cells were stimulated with anti-CD3 monoclonal antibody OKT3 (5 μg/ml) (BioLegend) overnight. Human tonsil cells were derived from deidentified tonsils collected by S. Goudy of Emory University under an IRB-approved protocol, and used in the study as completely deidentified samples. The tonsil mononuclear cells were isolated as reported earlier (*71*) and plated in a 10-cm petri dish at a seeding density of 8×10^5 cells/ml. The plated cells were stimulated overnight with inactivated H1N1 virus (10 μg/ml) (Bio-Rad, PIP021) at 37°C in an incubator. The live follicular helper T cells were sorted from tonsil mononuclear cells with biomarkers CD4$^+$ (BD Biosciences, 563550), CXCR5$^+$ (Thermo Fisher Scientific, 25-9185-42), PD1$^+$ (BioLegend, 329908), and live/dead blue using BD Fusion sorter. To study how cytoskeleton perturbation affects force generation, Farage B cells were treated with either 200 nM latrunculin A for 1 hour, 10 μM Y-26732 for 1 hour, or 5 μM blebbistatin for 5 min in complete medium immediately before imaging.

Soluble CD40L constructs and other proteins

Soluble WT CD40L (CD154) gene (TNF homology region M113-L261) including an N-terminal 6× His-tag and Avi-Tag was synthesized and purchased from Twist Bioscience and subcloned into the pHR-CMV-TetO2_3C-Avi-His6__IRES-EmGFP vector (a gift from A. R. Aricescu, Addgene plasmid #113888) by in vivo assembly (IVA) at the Age I and Xho I sites. Mutations to the WT CD40L gene were obtained by site-directed mutagenesis using primers purchased from Integrated DNA Technologies and KLD enzyme mix purchased from New England Biolabs (Ipswich, MA). The sequence of the cloned genes was verified by whole-plasmid nanopore sequencing from Plasmidsaurus and Sanger sequencing of insert from Eurofins Genomics. Lentiviruses encoding for all CD40L constructs were generated by polyethylenimine transfection of HEK293T/17 cells (ATCC) with the CD40L transfer vectors as well as packaging and envelope plasmids, psPAX2 and pMD2.G (gifts from D. Trono, Addgene plasmids #12260 and #12259). Lentiviral particles were harvested from the supernatant and concentrated 100× using polyethylene glycol (PEG) precipitation, using the Lenti-X concentrator (Takara Bio). Stable expression of soluble CD40L constructs was generated by lentiviral transduction of HEK293T/17 cells expressing BirA enzyme for in vivo biotinylation. His-tagged CD40L proteins were harvested from cell supernatant and purified by Ni-NTA chromatography. After purification, soluble proteins were buffer exchanged and concentrated using Amicon Ultra-15 10K Centrifugal Filter units (MilliporeSigma) and stored in phosphate-buffered saline (PBS) + 30% glycerol for further use after snap freezing in liquid nitrogen. Purified proteins were then verified by SDS-PAGE (fig. S1A) as well as by capturing proteins on streptavidin beads and immunocytometry (fig. S1B) with anti-CD40L and anti-His tag antibodies (BioLegend), and compared to commercial soluble CD40L (ACROBiosystems).

Recombinant human biotinylated CD40-Fc was purchased from ACROBiosystems, human IL-4 and IL-21 were purchased from PeproTech, and BAFF was purchased from R&D Systems. Phycoerythrin (PE) anti-human CD154, PE anti-human CD40, biotin anti-human CD40, PE anti-human CD19, APC anti-human CD38 antibody, PE/Cy7 anti-human CD27, BV605 anti-human IgM, and FITC anti-human IgG Fc antibodies were purchased from BioLegend. PE p-p38 mitogen-activated protein kinase (MAPK) (Thr^{180}/Tyr^{182}), PE p44/42 MAPK (Erk1/2) (Thr^{202}/Tyr^{204}), and anti-human TFEB (D2O7D) antibodies were purchased from Cell Signaling Technology. PE anti-His6× tag antibody was purchased from Novus Biologicals, anti-human IgM-F(ab′)$_2$ fragment antibody from Jackson Immune Research Lab, and FITC anti-rabbit IgG from BD Biosciences.

BFP measurement

BFP setup

Our custom-designed and homebuilt BFP has previously been described (*43*, *105*, *106*) and was used in this study to measure the 2D kinetics of bonds between a panel of soluble CD40L constructs or anti-CD40 antibody and either soluble and membrane-bound CD40 in the absence of force by the adhesion frequency assay (*35*, *37*) and in the presence of force by the force-clamp assay (*45*, *48*). In brief, we coated streptavidin-conjugated glass beads with soluble CD40L constructs or anti-CD40 antibody using biotin-streptavidin coupling. We then attached a functionalized bead to the apex of a biotinylated RBC aspirated by a glass micropipette to form a force transducer (probe), which has millisecond (time), nanometer (position), and piconewton (force) resolutions (*43*, *106*). Such a force probe was used to test binding with CD40 expressed on lymphoma or PBMC B cells (targets) in repeated mechanical cycles (fig. S1C). In some experiments, soluble CD40-Ig Fc was captured by an anti-Fc antibody covalently linked to a glass bead. To covalently link

anti-Fc to glass beads, glass beads were first thiolated with (3-mercaptopropyl)trimethoxysilane (MilliporeSigma), and then anti-Fc antibody was reacted with the bifunctional polymer $SM(PEG)_2$ (Thermo Fisher Scientific) for 30 min at room temperature, followed by removal of unreacted $SM(PEG)_2$ by centrifugal filtration. Thiolated beads were then incubated overnight at 4°C with the maleimide-functionalized anti-Fc antibody. All measurements were conducted in the chamber buffer (L15 with 1% BSA and 5 mM Hepes) at room temperature.

Adhesion frequency assay

During each mechanical cycle, we drove the target aspirated on the right micropipette (Fig. 1, B and C) using a piezo translator controlled by a computer program to approach and briefly (0.1 to 5 s) contact the probe held by the left micropipette (Fig. 1, B and C) with a small impingement force (~20 pN) to allow bond formation, followed by retraction of the target away from the probe at a force loading rate of 1000 pN/s. This generates a binary readout: either a binding event manifesting a positive force (tension) upon retraction or a no binding event manifesting the return of negative force (compression) (fig. S1C, bottom right). We estimated the adhesion frequency (P_a = # binding events divided by total # of contacts) from repeated mechanical cycles of the same contact time (t_c) using the same probe-target pair, converted P_a to average number of bonds per contact by a logarithmic transformation $\langle n\rangle = -\ln(1-P_a)$, divided the value by the site densities of CD40 (m_{CD40}) and CD40L (m_{CD40L}) measured by independent flow cytometry experiment, obtained mean ± SEM values using three to four probe-target pairs, measured these for a range of contact times, and fitted the data to a previously published model (*35*): $\langle n\rangle/m_{CD40}m_{CD40L} = A_cK_{a,}0(1-e^{-k_{off,0}t_c})$ to evaluate the apparent effective 2D affinity $A_cK_{a,0}$ (in μm^4) and off-rate $k_{off,0}$ (in s^{-1}), where A_c (in μm^2) is the contact area whose exact value is difficult to determine precisely but was kept constant for each probe-target system. For this reason, we lump it together with $K_{a,0}$ and add an adjective "effective" to distinguish $A_cK_{a,0}$ from the 2D affinity $K_{a,0}$ (in μm^2). Another adjective apparent is added here to distinguish $A_cK_{a,0}$ from the intrinsic binding affinity or affinities in the (to-be-determined) more realistic kinetic model than our previous published model (*35*) for the real CD40-CD40L interaction on the cell membrane, which is likely multivalent as opposed to monomeric as assumed here. For the same reason, caution must be exercised in comparing $A_cK_{a,0}$ values measured from different systems, e.g., bead-bead (see Fig. 1B) and bead-cell (see Fig. 1C) experiments or bead-cell experiments with different cells, even for the same molecular interactions because their contact areas and multivalencies may not be the same. Also note that the subscript 0 associated with the two binding parameters to indicate that the $K_{a,0}$ and $k_{off,0}$ values are measured under zero-force conditions (*35*).

Force-clamp assay

In the retraction phase of the mechanical cycle, if a bond survived the ramping and reached a preset tension level, the force was clamped until spontaneous bond dissociation and a pair of values of the clamped force f and bond lifetime t_b were measured (fig. S1C, top right). To ensure that most adhesion events were mediated by single molecular bonds, we controlled the adhesion to be infrequent (≤20%) (*35*). Bond lifetimes were measured at forces ranging from 2 to 45 pN, pooled, and binned into >5 force bins (>35 measurements per bin) to reduce system errors, and presented as mean ± SEM bond lifetime $\langle t_b\rangle$. The SEM of mean force is usually smaller than the size of the symbols in the plots, which is obscured.

MTP experiment

We functionalized DNA-based MTP on glass coverslips using a protocol adapted from previous publications (*52*, *53*). In brief, 25-mm glass coverslips were sonicated in 50% ethanol for 15 min and rinsed 6× with di-H_2O. Following rinsing, the coverslips were etched in 40-ml Piranha solution (2:1 ratio of sulfuric acid to H_2O_2) for 30 min. Coverslips were washed 6× with di-H_2O and 3× with 100% ethanol. The surfaces were then silanized with 3% 3-aminopropyltriethoxysilane in ethanol for 1 hour, then washed 3× in ethanol, and dried at 80°C for 30 min. After drying, 200 μl of lipoic acid-polyethylene glycol (10 mg/ml) and polyethylene glycol monomethyl ether (50 mg/ml) in 0.1 M $NaHCO_3$ was added to each surface and incubated overnight at 4°C. Surfaces were then washed 3× with di-H_2O, and 200 μl of sulfo–*N*-hydroxysuccinimide (NHS)–acetate (1 mg/ml) was added to two coverslips placed together as a sandwich and incubated for 30 min at room temperature. Coverslips were again rinsed 3× with di-H_2O, and 500 μl of AuNP solution was added to each sandwich and incubated for 1 hour at room temperature. During AuNP incubation, 300 nM hairpin strand, 330 nM quencher strand, and 330 nM Atto647 strand in 1 M NaCl were annealed in a thermocycler by heating to 95°C for 5 min and gradually cooling (−5°C/min) to 25°C. After rinsing AuNP-coated surfaces with 3× di-H_2O and 2× 1 M NaCl washes, 100 μl of DNA probes was added to each sandwich and incubated overnight at 4°C. The following day, the MTP coverslips were rinsed with 3× PBS washes and streptavidin (40 μg/ml) in PBS was added to each sandwich and incubated for 1 hour at room temperature. Following 3× rinse with PBS, biotinylated CD40L construct (40 μg/ml), anti-CD40 antibody, soluble CD40, or BSA in PBS + 2% (unbiotinylated) BSA was added to each sandwich and incubated for 1 hour at room temperature. For B cell MTP time course and cytoskeleton inhibition experiments, as well as T cell MTP experiments, MTP surfaces were prepared inside microfluidic channels. Briefly, 25 × 75 mm^2 coverslips were sonicated, etched, and silanized as described above for and then dried under argon stream after 3× ethanol washes. After drying, one Ibidi Sticky-Slide VI 0.4 was mounted on each coverslip to create six microfluidic channels per coverslip while making sure to remove any bubbles from the adhesive areas. NHS-PEG4-azide was then diluted in 0.1 M $NaHCO_3$ to 10 mg/ml, and 50 μl of the solution was added to each channel and incubated at room temperature for 1 hour. The channels were then washed 3× with 1 ml of di-H_2O and blocked with PBS + 1% BSA for 1 hour. During this incubation, 200 nM hairpin strand, 220 nM dibenzocyclooctyne (DBCO) quencher strand, and 220 nM Atto647 strand were annealed in 1 M NaCl in a thermocycler by heating to 95°C for 5 min and gradually cooling (−5°C/min) to 25°C. After blocking, the channels were washed 3× with PBS and 50 μl of PBS was left in the channels to prevent drying. The MTP probes were then added (50 μl) to each channel and incubated overnight at room temperature to covalently functionalize the channels with MTP probes via strain-promoted alkyne-azide cycloaddition (SPAAC). The following day, channels were rinsed 3× with PBS, and 50 μl of streptavidin solution (20 μg/ml) in PBS was added to each channel and incubated for 1 hour at room temperature. After rinsing 3× with PBS, 50 μl of biotinylated CD40L (40 μg/ml) [or 50 μl of biotinylated CD40-Fc (40 μg/ml)] in PBS + 1% BSA was added to each channel and incubated for 1 hour at room temperature.

TGT surface experiment

To prepare TGT surfaces, 25 × 75 mm^2 coverslips were sonicated, etched, and silanized as described above for MTP and then dried under argon stream after 3× ethanol washes. After drying, one Ibidi Sticky-Slide VI 0.4 was mounted on each coverslip to create six microfluidic channels per coverslip while making sure to remove any bubbles from the adhesive areas. NHS-PEG4-azide was then diluted in 0.1 M $NaHCO_3$ to 10 mg/ml, and 50 μl of the solution was added to each channel and incubated at room temperature for 1 hour. The channels were then washed 3× with 1 ml of di-H_2O and blocked with PBS + 1% BSA for 1 hour. During this incubation, the DBCO-bottom strand and the biotin-top strand of TGT probes (220 nM each in 1 M NaCl) were annealed in a thermocycler by heating to 95°C for 5 min and gradually cooling (−5°C/min) to 25°C. After blocking, the channels were washed 3× with PBS and 50 μl of PBS was left in the channels to prevent drying. The TGT probes were then added (50 μl) to each channel and incubated overnight at room temperature to covalently functionalize the channels with the TGT probes. The following day, channels were rinsed 3× with PBS, and 50 μl of streptavidin solution (20 μg/ml) in PBS was added to each channel and incubated for 1 hour at room temperature. After rinsing 3× with PBS, 50 μl of biotinylated CD40L (20 μg/ml) in PBS + 1% BSA was added to each channel and incubated for 1 hour at room temperature.

TGT bead experiment

TGT probes were heat annealed as described above (220 nM in 1 M NaCl for each strand, 1 ml in a thermocycler). After annealing, the required amount of azide-coated poly(methacrylic acid) (PMMA) beads (12 μm, PolyAn) for a 1:1 cell:bead ratio was washed 2× with PBS + 2% BSA by centrifugation at 200*g* for 3 min, then resuspended in the TGT probe solution (~1 ml), and incubated overnight on rotor at room temperature to allow functionalization of the beads with the TGT probes by SPAAC click reaction. The following day, TGT-coated beads were washed 2× with PBS + 2% BSA and resuspended in 500 μl of streptavidin (40 μg/ml) in PBS + 2% BSA and incubated for 1 hour on rotor at room temperature. After washing 2× with PBS + 2% BSA, beads were resuspended in biotinylated CD40L [1 μg/ml (for Farage B cells) or 3 μg/ml (for PBMC B cells)] in PBS + 2% BSA and incubated for 1 hour at room temperature. TGT beads were then washed 2× in PBS + 2% BSA to remove free CD40L before use. PBMC or Farage B cells were then seeded together with TGT beads in a 96-well plate at a seeding density of 75,000 B cells per well and a 1:1 cell-to-bead ratio, and incubated at 37°C. Cells and beads were then harvested at given time points, fixed in 4% paraformaldehyde (PFA), permeabilized with 90% methanol, and stained with either PE anti–p-p38 or PE anti–p-Erk1/2 antibodies (1:50 dilution) for 30 min at room temperature with gentle shaking. Phosphorylation of p38 and Erk1/2 was then measured by flow cytometry, gated for single cells, and quantified by mean fluorescence intensity (MFI) or the PE channel.

Fluorescence microscopy

MTP and TGT surfaces were imaged on a Nikon Eclipse Ti2-E microscope equipped with a Hamamatsu ORCA-Fusion Gen-III sCMOS camera, four laser excitation lines (405/488/561/640 nm, 20 mW), Nikon's motorized total internal reflection fluorescence (TIRF) illuminator, a reflection interference contrast microscopy (RICM) C-FL SRIC filter set, and a CFI Apo TIRF 60× Oil 1.49 NA (numerical aperture) objective. For each image, TIRF, RICM, and differential interference contrast (DIC) channels were recorded. TIRF images of MTP were recorded using the 640-nm laser (70% power, 300-ms exposure time). For time-lapse experiments, TIRF and RICM images were captured every 10 s for a total duration of 20 min, using Nikon's perfect focus system (PFS) to avoid loss of focus over time. MTP and TGT images were analyzed using custom software (see Data and materials availability). Briefly, for both MTP and TGT experiments, single cells were segmented based on the DIC channel, and then the cell spreading for each single cell was segmented based on the RICM channel. For MTP experiments, the TIRF 640-nm channel was background subtracted and the fluorescent intensity of the Atto647 signal was integrated over the spreading area of each single cell.

PMFA assay

To apply magnetic force in a parallel fashion across all wells of a 24-well plate, we designed, in Solidworks, a lid that would fit the top of a 24-well plate with two slots per well to house magnets and 3D printed it out of polylactic acid (PLA) filament. Using such a lid, we mounted two 5-mm cube neodymium magnets in antiparallel configuration per well, making sure that all magnets on the lid are mounted following exactly the same antiparallel pattern to allow reproducible force application to all wells. The magnetic lid could then be sterilized by immersion in 70% EtOH and then dried under argon stream. Next, to the center of each well of a non–tissue culture–treated 24-well plate, we applied a droplet of 5-min epoxy using a pipette tip. At the same time, 5-mm-diameter glass coverslips were cleaned by sequential washes in 70% EtOH and di-H_2O. Using a pair of tweezers, each coverslip was then dried by gentle tapping of its side on a kimwipe and gently placed on top of the epoxy droplet in the center of the well. To aid this process, it is helpful to mark the center of each well on the back side of the well plate and to proceed by applying epoxy and adding coverslips row by row, as waiting too long will result in the epoxy hardening and the inability to attach the coverslips to the plate. After attaching coverslips to the center of every well, the wells were washed with 1 ml of PBS, and then PBS was added again to each well (~1 ml) and the plate was incubated for 30 min at room temperature. Following incubation, PBS was thoroughly aspirated out of each well, and plates were then left to air dry completely for 30 min at room temperature. After wells and coverslips were fully dried, an 18-μl droplet of 0.01% PLL solution (Sigma-Aldrich) was carefully added to each coverslip, and plates were incubated at 4°C overnight to allow coating of PLL on the glass coverslips. The following day, wells were washed with ~1 ml of PBS and dried by aspiration, making sure that the area around and underneath the coverslips is fully dried. After drying, 18 μl of B cells in R10 (1×10^5 to 2×10^5 cells/18 μl) was added on top of each coverslip and incubated for 10 min at 37°C to allow cells to settle and become immobilized on the PLL-coated coverslips. After immobilization, 2 μl of a well-mixed solution of CD40L-coated magnetic beads in R10 was carefully added on top of the R10 droplet above the immobilized cells at the center of every well. Plates were then incubated for 10 min at 37°C to allow the beads to sediment on the cells by gravity and to start interacting with B cells. After beads were settled, 80 μl of R10 (with supplements or treatments depending on the specific assay) was added to each well around the coverslip. Critically, care must be taken while adding the 80 μl of R10 to each well such that the coverslips and cells are not touched and that the flat droplet of medium does not contact the side walls of the well, which would

result in meniscus formation and unwanted drying of the sample. We found that adding 80 μl of medium slowly while making circular motions around the coverslip led to best results. After incubation for 10 min at 37°C, the magnetic lid was gently placed on top of the plates (or a normal lid without magnets for control samples), making sure that the magnets do not directly contact the top of the medium droplet, and cells were incubated under force application for a given period of time depending on the specific experiment.

Designing magnetic force profile in PMFA assay

To design the configuration of magnet lid and chamber to generate a well-defined magnetic force on magnetic beads in a defined space requires a defined magnetic field gradient. Positive magnetophoresis is a phenomenon that occurs when magnetic objects (e.g., magnetic beads) have positive magnetization vectors and are immersed in nonmagnetic substances such as buffer, cells, or tissues. In this context, a relative magnetic permeability μ_r^b ($\equiv\mu_b/\mu_0$, where μ_b and μ_0 are the permeability values of the magnetic particle and of vacuum, respectively) is always higher than that of buffer, cells, or tissues (which is essentially nonmagnetic, i.e., $\mu_m \approx \mu_0$). In the presence of a gradient in the external magnetic field, these magnetic objects tend to be attracted to spaces with denser magnetic fields and higher field gradients. For a spherical magnetic particle, the magnetic force $\vec{F}$ is given by

$$\vec{F} = \mu_0 V\left(\overrightarrow{M}\cdot\nabla\right)\vec{B} \quad (1)$$

where $\overrightarrow{M}$ is the magnetization strength of a particle per unit volume, V is the volume of the magnetic particle, and $\vec{B}$ is the applied external magnetic field strength in the surrounding medium. Since we used a superparamagnetic bead that has minimal residual magnetization, the magnetic force can be exerted on the beads only when there is an external magnetic field. If the magnetic field itself is strong enough, by Langevin's theory of paramagnetism, the magnetization strength vector reaches saturation, resulting in $\overrightarrow{M} = \overrightarrow{M}_s$, the saturated magnetization per unit volume. Hence, the magnetic force can be reduced to simple form such that $\vec{F} = \frac{4}{3}\pi R_{bead}^3 M_{ms}\rho_{bead}\nabla|B|$, where ρ_{bead} is the density of a magnetic bead (1.4 g/cm^3 for M270), R_{bead} is the radius of a magnetic bead (1.4 μm for M270), and M_{ms} is the magnitude of mass saturation magnetization (10.88 J T^{-1} kg^{-1} for M270) (*107*–*109*). To calculate the magnetic field, in the absence of both electric fields and external currents, the magneto-static state for hard ferromagnets (two permanent neodymium magnets with a magnetization grade of N50) with a 1-mm gap in between can be described as

$$\overrightarrow{\nabla}\times\left(\vec{B}/\mu_0-\overrightarrow{M}\right)=0 \quad (2)$$

where $\overrightarrow{M}$ is the strength of magnetization from the remanent field ($\overrightarrow{B_r}/\mu_0$ for B_r = 1.24 T for a pair of two N50-grade magnets) (*110*). Using the above equations, due to the finite size constraint of medium in each well of a 24-well plate, we calculated the magnetic force profile under the circumstance where each pair of magnets is placed as low as possible (1.5 mm from the surface) inside the wells.

PMFA for intracellular signaling

For this experiment, PMFA plates, cells, and beads were prepared as described above, adding 2×10^5 cells per well. Beads were functionalized with CD40L (1 μg/ml) for Farage cells or CD40L (3 μg/ml) for PBMC B cells. In the samples treated with soluble CD40L, an equivalent amount of CD40L was added to each well as that of CD40L coated on beads (2 μl of 1 or 3 μg/ml for Farage or PBMC B cells, respectively). Following preset incubation times (0, 0.5, 1, 3, or 5 hours), cells were harvested by trypsinization (500 μl of TrypLE, Gibco) for 5 min at 37°C, followed by 1 ml of R10. Cells were then washed with PBS and fixed in 1 ml of PBS with 4% PFA for 10 min at 37°C. After fixation, cells were permeabilized by adding the cells to 9 ml of ice-cold 100% methanol to a final concentration of 90% methanol and incubated on ice for 30 min. Cells were then washed 2× in 1 ml of fluorescence-activated cell sorting (FACS) buffer and resuspended in 50 to 100 μl of 1:50 diluted primary PE-conjugated antibodies against phosphorylated p38 or Erk1/2 (Cell Signaling Technology) and stained for 1 hour at room temperature on a rotor. After staining, cells were washed twice in 1 ml of FACS buffer and resuspended in 0.2 to 0.3 ml of FACS buffer for flow cytometry analysis.

PMFA for TFEB translocation

In this experiment, PMFA plates and magnetic beads were prepared as described above. Ramos cells (2.5×10^5 cells per well) were added to each coverslip with the addition of anti-IgM (8 μg/ml) for BCR stimulation. Beads coated with CD40L (0.2 μg/ml) were then added to each well as described above, and cells were incubated under magnetic force application for 1 hour. After incubation, cells were harvested by trypsinization as described above, and four wells were combined for each sample to reach 1×10^6 cells per sample. After washing with 500 μl of PBS by centrifuging at 300*g* for 5 min, cells were fixed with 500 μl of 1:1 mixture of PBS and CytoFix buffer (BD) for 20 min at room temperature. After fixing, cells were washed with 1 ml of FACS buffer by centrifuging at 700*g* for 5 min at 4°C and then permeabilized and stained in 150 μl of FACS buffer + 0.1% Triton X-100 with primary anti-TFEB antibody (1:150 dilution) for 30 min at 4°C in the dark. Fixed cells were washed 2× with 1 ml of FACS buffer by centrifuging at 700*g* for 5 min at 4°C and stained with secondary anti-rabbit FITC antibody in FACS buffer (1:150 dilution) for 30 min at 4°C in the dark. Cells were then washed 2× in 1 ml of FACS buffer by centrifuging at 700*g* for 5 min at 4°C and resuspended in 30 μl of FACS buffer containing 7-AAD (10 μg/ml) for nuclear staining. Cells were then imaged with the ImageStream cytometer in the bright-field, FITC, and 7-AAD channels at ×60 magnification and gated for in-focus and live cells.

PMFA for class-switch recombination

In the first 6 hours of this experiment, we stimulated PBMC B cells using the PMFA setup described above. Specifically, we immobilized 10^5 PBMC B cells on PLL-coated coverslips in an 18-μl R10 droplet and added 2 μl of magnetic beads coated with CD40L (0.2 to 0.6 μg/ml coating) to each well at a 1:2 cell to bead ratio (2×10^5 beads per well). After addition of the beads, 80 μl of R10 supplemented with BAFF (100 ng/ml) and IL-4 (20 ng/ml) (final concentration) was added around the coverslips to form a 100-μl droplet as described above. Following a brief incubation for 10 min at 37°C, magnetic lids were placed above the plates containing samples to be stimulated under magnetic force, and cells were incubated for 6 hours under force. After this 6-hour incubation, magnetic lids were removed, 400 μl of R10 supplemented with BAFF (100 ng/ml) and IL-4 (20 ng/ml) was added to each well (500 μl total volume), and all cells and beads were transferred to new 24-well plates for prolonged stimulation without force to elicit GC formation. After 4 days, plates were

centrifuged at 450*g* for 5 min, and 250 μl of the conditioned medium was removed from the top of each well, making sure that cells and beads were not aspirated. R10 (500 μl) supplemented with BAFF (100 ng/ml) and IL-21 (10 ng/ml) was then added to each well, and cells were further incubated with beads for 4 days at 37°C. On day 8, cells were harvested and washed twice with 200 μl of FACS buffer after transferring to a 96-well plate by centrifuging at 500*g* for 5 min. After washing, dead cells were stained with 100 μl of LIVE/DEAD Fixable stain (Thermo Fisher Scientific) at 1000× dilution in PBS for 30 min at room temperature in the dark with shaking. Cells were then washed twice in 200 μl of FACS buffer by centrifuging at 500*g* for 5 min and resuspended in 100 μl of FACS buffer containing the following antibody cocktail: anti-CD27, anti-CD38, anti-IgM, anti-IgG (all 1:200 dilution), and anti-CD19 (1:100 dilution). Cells were thus stained for 1 hour at room temperature in the dark with shaking. After staining, cells were washed 2× with 200 μl of FACS buffer by centrifuging at 500*g* for 5 min and then fixed in 100 μl of PBS with 4% PFA for 30 min at room temperature in the dark with shaking. Following fixation, PFA was removed by 2× washes with 200 μl of FACS buffer by centrifuging at 600*g* for 5 min, and cells were resuspended in 200 μl of FACS buffer and stored at 4°C in the dark until flow cytometry analysis. Flow cytometry gating was determined based on FMO control for each fluorophore.

Analysis of image flow cytometer

All images obtained from the Amnis ImageStream were exported to Matlab and converted to Tiff format for further analysis of TFEB translocation. The raw data format consists of one cell per image and includes four channels: bright-field, side scatter, FITC (for TFEB), and 7-AAD (for nucleus). First, the nucleus was segmented based on the 7-AAD channel by applying adaptive threshold to binarize the raw image. Similarly, each entire cell was segmented based on the FITC channel. After segmenting both whole cell and nucleus, the mean background fluorescence was subtracted from each TFEB and 7-AAD image. To calculate the similarity index between the TFEB channel and the nucleus channel, we computed the Pearson's coefficient (p) between the two channels for the whole-cell segmented area (thus excluding the background pixels from the calculation). The Pearson's coefficient between two images x and y is defined as

$$p = \frac{\sum (x-\bar{x})(y-\bar{y})}{\sqrt{\sum (x-\bar{x})^2}\sqrt{\sum (y-\bar{y})^2}} \quad (3)$$

where $\bar{x}$ and $\bar{y}$ are the mean pixel values of each image. The Pearson's coefficient is a dimensionless value between −1 and 1 representing the linear correlation between the pixel values of the two images, where 1, −1, and 0 indicate perfect correlation, perfect inverse correlation, and no correlation, respectively. To address the low dynamic range of the Pearson's coefficient, another metric has been defined as a monotonic function of the Pearson's coefficient, the similarity score (S)

$$S = \ln\left[\frac{1+p}{1-p}\right] \quad (4)$$

The similarity score effectively rescales the Pearson's coefficient from $-\infty$ to $+\infty$, allowing for more accurate measurements of similarity between the two channels. Next, to determine the portion of cells with nuclear TFEB, a gate was applied to the similarity score distribution, with a threshold set at 1. Thus, cells with a similarity score of >1 were identified as having nuclear TFEB, while cells with a score of <1 were classified as having cytosolic TFEB.

Data and statistical analysis

Results are presented as either mean ± SD or mean ± SEM, or mean only wherever applicable. *P* values were calculated by unpaired, two-sided *t* test with labeling convention of ns > 0.05, $*P \leq 0.05$, $**P \leq 0.01$, $***P \leq 0.001$, and $****P \leq 0.0001$. Custom LabView and MATLAB software was written for analysis of BFP and MTP data. Data obtained from TGT and PMFA assays were analyzed using FlowJo and MATLAB software. Statistical details have also been provided in figure legends and in Materials and Methods where applicable.

Supplementary Materials

The PDF file includes:
Figs. S1 to S8
Legend for movie S1

Other Supplementary Material for this manuscript includes the following:
Movie S1

REFERENCES AND NOTES

1. R. Elgueta, M. J. Benson, V. C. De Vries, A. Wasiuk, Y. Guo, R. J. Noelle, Molecular mechanism and function of CD40/CD40L engagement in the immune system. *Immunol. Rev.* **229**, 152–172 (2009).
2. M. Akkaya, J. Traba, A. S. Roesler, P. Miozzo, B. Akkaya, B. P. Theall, H. Sohn, M. Pena, M. Smelkinson, J. Kabat, E. Dahlstrom, D. W. Dorward, J. Skinner, M. N. Sack, S. K. Pierce, Second signals rescue B cells from activation-induced mitochondrial dysfunction and death. *Nat. Immunol.* **19**, 871–884 (2018).
3. T. J. Ripperger, D. Bhattacharya, Transcriptional and metabolic control of memory B cells and plasma cells. *Annu. Rev. Immunol.* **39**, 345–368 (2021).
4. N. A. Mitchison, T-cell-B-cell cooperation. *Nat. Rev. Immunol.* **4**, 308–312 (2004).
5. J. G. Cyster, C. D. C. Allen, B cell responses: Cell interaction dynamics and decisions. *Cell* **177**, 524–540 (2019).
6. J. Boisvert, S. Edmondson, M. F. Krummel, Immunological synapse formation licenses CD40-CD40L accumulations at T-APC contact sites. *J. Immunol.* **173**, 3647–3652 (2004).
7. I. Berberich, G. L. Shu, E. A. Clark, Cross-linking CD40 on B cells rapidly activates nuclear factor-kappa B. *J. Immunol.* **153**, 4357–4366 (1994).
8. I. Papa, C. G. Vinuesa, Synaptic interactions in germinal centers. *Front. Immunol.* **9**, 1858 (2018).
9. B. O. Lee, J. Moyron-Quiroz, J. Rangel-Moreno, K. L. Kusser, L. Hartson, F. Sprague, F. E. Lund, T. D. Randall, CD40, but not CD154, expression on B cells is necessary for optimal primary B cell responses. *J. Immunol.* **171**, 5707–5717 (2003).
10. Z. Shulman, A. D. Gitlin, J. S. Weinstein, B. Lainez, E. Esplugues, R. A. Flavell, J. E. Craft, M. C. Nussenzweig, Dynamic signaling by T follicular helper cells during germinal center B cell selection. *Science* **345**, 1058–1062 (2014).
11. J. Jacob, G. Kelsoe, K. Rajewsky, U. Weiss, Intraclonal generation of antibody mutants in germinal centres. *Nature* **354**, 389–392 (1991).
12. Z. Li, C. J. Woo, M. D. Iglesias-Ussel, D. Ronai, M. D. Scharff, The generation of antibody diversity through somatic hypermutation and class switch recombination. *Genes Dev.* **18**, 1–11 (2004).
13. J. A. Roco, L. Mesin, S. C. Binder, C. Nefzger, P. Gonzalez-Figueroa, P. F. Canete, J. Ellyard, Q. Shen, P. A. Robert, J. Cappello, H. Vohra, Y. Zhang, C. R. Nowosad, A. Schiepers, L. M. Corcoran, K.-M. Toellner, J. M. Polo, M. Meyer-Hermann, G. D. Victora, C. G. Vinuesa, Class-switch recombination occurs infrequently in germinal centers. *Immunity* **51**, 337–350.e7 (2019).
14. M. D. Jumper, J. B. Splawski, P. E. Lipsky, K. Meek, Ligation of CD40 induces sterile transcripts of multiple Ig H chain isotypes in human B cells. *J. Immunol.* **152**, 438–445 (1994).
15. G. D. Victora, T. A. Schwickert, D. R. Fooksman, A. O. Kamphorst, M. Meyer-Hermann, M. L. Dustin, M. C. Nussenzweig, Germinal center dynamics revealed by multiphoton microscopy with a photoactivatable fluorescent reporter. *Cell* **143**, 592–605 (2010).
16. A. D. Gitlin, Z. Shulman, M. C. Nussenzweig, Clonal selection in the germinal centre by regulated proliferation and hypermutation. *Nature* **509**, 637–640 (2014).
17. A. E. Hauser, T. Junt, T. R. Mempel, M. W. Sneddon, S. H. Kleinstein, S. E. Henrickson, U. H. von Andrian, M. J. Shlomchik, A. M. Haberman, Definition of germinal-center B cell

migration in vivo reveals predominant intrazonal circulation patterns. *Immunity* **26**, 655–667 (2007).
18. R. C. Allen, R. J. Armitage, M. E. Conley, H. Rosenblatt, N. A. Jenkins, N. G. Copeland, M. A. Bedell, S. Edelhoff, C. M. Disteche, D. K. Simoneaux, CD40 ligand gene defects responsible for X-linked hyper-IgM syndrome. *Science* **259**, 990–993 (1993).
19. A. Aruffo, M. Farrington, D. Hollenbaugh, X. Li, A. Milatovich, S. Nonoyama, J. Bajorath, L. S. Grosmaire, R. Stenkamp, M. Neubauer, The CD40 ligand, gp39, is defective in activated T cells from patients with X-linked hyper-IgM syndrome. *Cell* **72**, 291–300 (1993).
20. S. Ferrari, S. Giliani, A. Insalaco, A. Al-Ghonaium, A. R. Soresina, M. Loubser, M. A. Avanzini, M. Marconi, R. Badolato, A. G. Ugazio, Y. Levy, N. Catalan, A. Durandy, A. Tbakhi, L. D. Notarangelo, A. Plebani, Mutations of CD40 gene cause an autosomal recessive form of immunodeficiency with hyper IgM. *Proc. Natl. Acad. Sci. U.S.A.* **98**, 12614–12619 (2001).
21. M. Muramatsu, K. Kinoshita, S. Fagarasan, S. Yamada, Y. Shinkai, T. Honjo, Class switch recombination and hypermutation require activation-induced cytidine deaminase (AID), a potential RNA editing enzyme. *Cell* **102**, 553–563 (2000).
22. K. Imai, G. Slupphaug, W.-I. Lee, P. Revy, S. Nonoyama, N. Catalan, L. Yel, M. Forveille, B. Kavli, H. E. Krokan, H. D. Ochs, A. Fischer, A. Durandy, Human uracil-DNA glycosylase deficiency associated with profoundly impaired immunoglobulin class-switch recombination. *Nat. Immunol.* **4**, 1023–1028 (2003).
23. R. Yazdani, S. Fekrvand, S. Shahkarami, G. Azizi, B. Moazzami, H. Abolhassani, A. Aghamohammadi, The hyper IgM syndromes: Epidemiology, pathogenesis, clinical manifestations, diagnosis and management. *Clin. Immunol.* **198**, 19–30 (2019).
24. J. Thusberg, M. Vihinen, The structural basis of hyper IgM deficiency–CD40L mutations. *Protein Eng. Des. Sel.* **20**, 133–141 (2007).
25. C. Thomas, G. De Saint Basile, F. Le Deist, D. Theophile, M. Benkerrou, E. Haddad, S. Blanche, A. Fischer, Correction of X-linked hyper-IgM syndrome by allogeneic bone marrow transplantation. *N. Engl. J. Med.* **333**, 426–429 (1995).
26. K. Kucka, H. Wajant, Receptor oligomerization and its relevance for signaling by receptors of the tumor necrosis factor receptor superfamily. *Front. Cell Dev. Biol.* **8**, 615141 (2021).
27. M. Grell, E. Douni, H. Wajant, M. Löhden, M. Clauss, B. Maxeiner, S. Georgopoulos, W. Lesslauer, G. Kollias, K. Pfizenmaier, P. Scheurich, The transmembrane form of tumor necrosis factor is the prime activating ligand of the 80 kDa tumor necrosis factor receptor. *Cell* **83**, 793–802 (1995).
28. M. Grell, H. Wajant, G. Zimmermann, P. Scheurich, The type 1 receptor (CD120a) is the high-affinity receptor for soluble tumor necrosis factor. *Proc. Natl. Acad. Sci. U.S.A.* **95**, 570–575 (1998).
29. A. Wyzgol, N. Müller, A. Fick, S. Munkel, G. U. Grigoleit, K. Pfizenmaier, H. Wajant, Trimer stabilization, oligomerization, and antibody-mediated cell surface immobilization improve the activity of soluble trimers of CD27L, CD40L, 41BBL, and glucocorticoid-induced TNF receptor ligand1. *J. Immunol.* **183**, 1851–1861 (2009).
30. K. L. Brunekreeft, C. Strohm, M. J. Gooden, A. A. Rybczynska, H. W. Nijman, G. U. Grigoleit, W. Helfrich, E. Bremer, D. Siegmund, H. Wajant, M. de Bruyn, Targeted delivery of CD40L promotes restricted activation of antigen-presenting cells and induction of cancer cell death. *Mol. Cancer* **13**, 85 (2014).
31. Y. Zeng, J. Yi, Z. Wan, K. Liu, P. Song, A. Chau, F. Wang, Z. Chang, W. Han, W. Zheng, Y.-H. Chen, C. Xiong, W. Liu, Substrate stiffness regulates B-cell activation, proliferation, class switch, and T-cell-independent antibody responses in vivo. *Eur. J. Immunol.* **45**, 1621–1634 (2015).
32. C. Zhu, W. Chen, J. Lou, W. Rittase, K. Li, Mechanosensing through immunoreceptors. *Nat. Immunol.* **20**, 1269–1278 (2019).
33. G. M. Vaitaitis, M. H. Olmstead, D. M. Waid, J. R. Carter, D. H. Wagner, CD40-targeted peptide proposed for type 1 diabetes therapy lacks relevant binding affinity to its cognate receptor. Reply to Pagni PP, Wolf A, Lo Conte M et al [letter]. *Diabetologia* **62**, 1730–1731 (2019).
34. G. I. Bell, Models for the specific adhesion of cells to cells. *Science* **200**, 618–627 (1978).
35. S. E. Chesla, P. Selvaraj, C. Zhu, Measuring two-dimensional receptor-ligand binding kinetics by micropipette. *Biophys. J.* **75**, 1553–1572 (1998).
36. M. L. Dustin, S. K. Bromley, M. M. Davis, C. Zhu, Identification of self through two-dimensional chemistry and synapses. *Annu. Rev. Cell Dev. Biol.* **17**, 133–157 (2001).
37. J. Huang, V. I. Zarnitsyna, B. Liu, L. J. Edwards, N. Jiang, B. D. Evavold, C. Zhu, The kinetics of two-dimensional TCR and pMHC interactions determine T-cell responsiveness. *Nature* **464**, 932–936 (2010).
38. A. Jain, T. P. Atkinson, P. E. Lipsky, J. E. Slater, D. L. Nelson, W. Strober, Defects of T-cell effector function and post-thymic maturation in X-linked hyper-IgM syndrome. *J. Clin. Invest.* **103**, 1151–1158 (1999).
39. L. D. Notarangelo, M. C. Peitsch, T. G. Abrahamsen, C. Bachelot, P. Bordigoni, A. J. Cant, H. Chapel, M. Clementi, S. Deacock, G. De Saint Basile, M. Duse, T. Espanol, A. Etzioni, A. Fasth, A. Fischer, S. Giliani, L. Gomez, L. Hammarstrom, A. Jones, M. Kanariou, C. Kinnon, T. Klemola, R. A. Kroczek, J. Levy, N. Matamoros, V. Monafo, P. Paolucci, I. Reznick, O. Sanal, C. I. E. Smith, R. A. Thompson, P. Tovo, A. Villa, M. Vihinen, J. Vossen, B. J. M. Zegers, H. D. Ochs, M. E. Conley, M. Iseki, N. Ramesh, M. Shimadzu, O. Saiki, CD40Lbase: A database of CD40L gene mutations causing X-linked hyper-IgM syndrome. *Immunol. Today* **17**, 511–516 (1996).
40. J. Bajorath, N. J. Chalupny, J. S. Marken, A. W. Siadak, J. Skonier, M. Gordon, D. Hollenbaugh, R. J. Noelle, H. D. Ochs, A. Aruffo, Identification of residues on CD40 and its ligand which are critical for the receptor-ligand interaction. *Biochemistry* **34**, 1833–1844 (1995).
41. H.-J. An, Y. J. Kim, D. H. Song, B. S. Park, H. M. Kim, J. D. Lee, S.-G. Paik, J.-O. Lee, H. Lee, Crystallographic and mutational analysis of the CD40-CD154 complex and its implications for receptor activation. *J. Biol. Chem.* **286**, 11226–11235 (2011).
42. A. Y. Sarode, M. K. Jha, S. Zutshi, S. K. Ghosh, H. Mahor, U. Sarma, B. Saha, Residue-specific message encoding in CD40-ligand. *iScience* **23**, 101441 (2020).
43. W. Chen, V. I. Zarnitsyna, K. K. Sarangapani, J. Huang, C. Zhu, Measuring receptor-ligand binding kinetics on cell surfaces: From adhesion frequency to thermal fluctuation methods. *Cell Mol. Bioeng.* **1**, 276–288 (2008).
44. E. Evans, K. Ritchie, R. Merkel, Sensitive force technique to probe molecular adhesion and structural linkages at biological interfaces. *Biophys. J.* **68**, 2580–2587 (1995).
45. B. Liu, W. Chen, B. D. Evavold, C. Zhu, Accumulation of dynamic catch bonds between TCR and agonist peptide-MHC triggers T cell signaling. *Cell* **157**, 357–368 (2014).
46. J. Hong, C. Ge, P. Jothikumar, Z. Yuan, B. Liu, K. Bai, K. Li, W. Rittase, M. Shinzawa, Y. Zhang, A. Palin, P. Love, X. Yu, K. Salaita, B. D. Evavold, A. Singer, C. Zhu, A TCR mechanotransduction signaling loop induces negative selection in the thymus. *Nat. Immunol.* **19**, 1379–1390 (2018).
47. H.-K. Choi, P. Cong, C. Ge, A. Natarajan, B. Liu, Y. Zhang, K. Li, M. N. Rushdi, W. Chen, J. Lou, M. Krogsgaard, C. Zhu, Catch bond models may explain how force amplifies TCR signaling and antigen discrimination. *Nat. Commun.* **14**, 2616 (2023).
48. B. T. Marshall, M. Long, J. W. Piper, T. Yago, R. P. McEver, C. Zhu, Direct observation of catch bonds involving cell-adhesion molecules. *Nature* **423**, 190–193 (2003).
49. P. Tolar, Cytoskeletal control of B cell responses to antigens. *Nat. Rev. Immunol.* **17**, 621–634 (2017).
50. E. Natkanski, W.-Y. Lee, B. Mistry, A. Casal, J. E. Molloy, P. Tolar, B cells use mechanical energy to discriminate antigen affinities. *Science* **340**, 1587–1590 (2013).
51. Z. Wan, X. Chen, H. Chen, Q. Ji, Y. Chen, J. Wang, Y. Cao, F. Wang, J. Lou, Z. Tang, W. Liu, The activation of IgM- or isotype-switched IgG- and IgE-BCR exhibits distinct mechanical force sensitivity and threshold. *eLife* **4**, e06925 (2015).
52. Y. Liu, L. Blanchfield, V. P.-Y. Ma, R. Andargachew, K. Galior, Z. Liu, B. Evavold, K. Salaita, DNA-based nanoparticle tension sensors reveal that T-cell receptors transmit defined pN forces to their antigens for enhanced fidelity. *Proc. Natl. Acad. Sci. U.S.A.* **113**, 5610–5615 (2016).
53. R. Ma, A. V. Kellner, V. P.-Y. Ma, H. Su, B. R. Deal, J. M. Brockman, K. Salaita, DNA probes that store mechanical information reveal transient piconewton forces applied by T cells. *Proc. Natl. Acad. Sci. U.S.A.* **116**, 16949–16954 (2019).
54. W. M. Morton, K. R. Ayscough, P. J. McLaughlin, Latrunculin alters the actin-monomer subunit interface to prevent polymerization. *Nat. Cell Biol.* **2**, 376–378 (2000).
55. T. Ishizaki, M. Uehata, I. Tamechika, J. Keel, K. Nonomura, M. Maekawa, S. Narumiya, Pharmacological properties of Y-27632, a specific inhibitor of rho-associated kinases. *Mol. Pharmacol.* **57**, 976–983 (2000).
56. S. Even-Ram, A. D. Doyle, M. A. Conti, K. Matsumoto, R. S. Adelstein, K. M. Yamada, Myosin IIA regulates cell motility and actomyosin–microtubule crosstalk. *Nat. Cell Biol.* **9**, 299–309 (2007).
57. X. Wang, T. Ha, Defining single molecular forces required to activate integrin and notch signaling. *Science* **340**, 991–994 (2013).
58. F. D. Batista, D. Iber, M. S. Neuberger, B cells acquire antigen from target cells after synapse formation. *Nature* **411**, 489–494 (2001).
59. T. Koike, K. Harada, S. Horiuchi, D. Kitamura, The quantity of CD40 signaling determines the differentiation of B cells into functionally distinct memory cell subsets. *eLife* **8**, e44245 (2019).
60. M. R. Gold, M. G. Reth, Antigen receptor function in the context of the nanoscale organization of the B cell membrane. *Annu. Rev. Immunol.* **37**, 97–123 (2019).
61. M. A. Fardin, O. M. Rossier, P. Rangamani, P. D. Avigan, N. C. Gauthier, W. Vonnegut, A. Mathur, J. Hone, R. Iyengar, M. P. Sheetz, Cell spreading as a hydrodynamic process. *Soft Matter* **6**, 4788–4799 (2010).
62. H. Wolfenson, T. Iskratsch, M. P. Sheetz, Early events in cell spreading as a model for quantitative analysis of biomechanical events. *Biophys. J.* **107**, 2508–2514 (2014).
63. P. A. Janmey, B. Hinz, C. A. McCulloch, Physics and physiology of cell spreading in two and three dimensions. *Phys. Ther.* **36**, 382–391 (2021).
64. A. Craxton, G. Shu, J. D. Graves, J. Saklatvala, E. G. Krebs, E. A. Clark, p38 MAPK is required for CD40-induced gene expression and proliferation in B lymphocytes. *J. Immunol.* **161**, 3225–3236 (1998).
65. K. Zhang, L. Zhang, D. Zhu, D. Bae, A. Nel, A. Saxon, CD40-mediated p38 mitogen-activated protein kinase activation is required for immunoglobulin class switch recombination to IgE. *J. Allergy Clin. Immunol.* **110**, 421–428 (2002).

66. R. K. Mathur, A. Awasthi, P. Wadhone, B. Ramanamurthy, B. Saha, Reciprocal CD40 signals through p38MAPK and ERK-1/2 induce counteracting immune responses. *Nat. Med.* **10**, 540–544 (2004).
67. A. Aicher, G. L. Shu, D. Magaletti, T. Mulvania, A. Pezzutto, A. Craxton, E. A. Clark, Differential role for p38 mitogen-activated protein kinase in regulating CD40-induced gene expression in dendritic cells and B cells. *J. Immunol.* **163**, 5786–5795 (1999).
68. J. Adem, A. Hämäläinen, A. Ropponen, J. Eeva, M. Eray, U. Nuutinen, J. Pelkonen, ERK1/2 has an essential role in B cell receptor- and CD40-induced signaling in an in vitro model of germinal center B cell selection. *Mol. Immunol.* **67**, 240–247 (2015).
69. Á. dos Santos, N. Fili, D. S. Pearson, Y. Hari-Gupta, C. P. Toseland, High-throughput mechanobiology: Force modulation of ensemble biochemical and cell-based assays. *Biophys. J.* **120**, 631–641 (2021).
70. M. Münchhalfen, R. Görg, M. Haberl, J. Löber, J. Willenbrink, L. Schwarzt, C. Höltermann, C. Ickes, L. Hammermann, J. Kus, B. Chapuy, A. Ballabio, S. D. Reichardt, A. Flügel, N. Engels, J. Wienands, TFEB activation hallmarks antigenic experience of B lymphocytes and directs germinal center fate decisions. *Nat. Commun.* **15**, 6971 (2024).
71. L. E. Wagar, A. Salahudeen, C. M. Constantz, B. S. Wendel, M. M. Lyons, V. Mallajosyula, L. P. Jatt, J. Z. Adamska, L. K. Blum, N. Gupta, K. J. L. Jackson, F. Yang, K. Röltgen, K. M. Roskin, K. M. Blaine, K. D. Meister, I. N. Ahmad, M. Cortese, E. G. Dora, S. N. Tucker, A. I. Sperling, A. Jain, D. H. Davies, P. L. Felgner, G. B. Hammer, P. S. Kim, W. H. Robinson, S. D. Boyd, C. J. Kuo, M. M. Davis, Modeling human adaptive immune responses with tonsil organoids. *Nat. Med.* **27**, 125–135 (2021).
72. P. L. Graney, Z. Zhong, S. Post, I. Brito, A. Singh, Engineering early memory B-cell-like phenotype in hydrogel-based immune organoids. *J. Biomed. Mater. Res.* **110**, 1435–1447 (2022).
73. T. D. Moeller, S. B. Shah, K. Lai, N. Lopez-Barbosa, P. Desai, W. Wang, Z. Zhong, D. Redmond, A. Singh, M. P. DeLisa, Profiling germinal center-like B cell responses to conjugate vaccines using synthetic immune organoids. *ACS Cent. Sci.* **9**, 787–804 (2023).
74. M. N. Rushdi, V. Pan, K. Li, H.-K. Choi, S. Travaglino, J. Hong, F. Griffitts, P. Agnihotri, R. A. Mariuzza, Y. Ke, C. Zhu, Cooperative binding of T cell receptor and CD4 to peptide-MHC enhances antigen sensitivity. *Nat. Commun.* **13**, 7055 (2022).
75. J. W. Piper, R. A. Swerlick, C. Zhu, Determining force dependence of two-dimensional receptor-ligand binding affinity by centrifugation. *Biophys. J.* **74**, 492–513 (1998).
76. J. Hong, S. P. Persaud, S. Horvath, P. M. Allen, B. D. Evavold, C. Zhu, Force-regulated in situ TCR-peptide-bound MHC class II kinetics determine functions of $CD4^+$ T cells. *J. Immunol.* **195**, 3557–3564 (2015).
77. N. S. De Silva, U. Klein, Dynamics of B cells in germinal centres. *Nat. Rev. Immunol.* **15**, 137–148 (2015).
78. J. Liu, N. J. Agrawal, A. Calderon, P. S. Ayyaswamy, D. M. Eckmann, R. Radhakrishnan, Multivalent binding of nanocarrier to endothelial cells under shear flow. *Biophys. J.* **101**, 319–326 (2011).
79. D. Hollenbaugh, L. S. Grosmaire, C. D. Kullas, N. J. Chalupny, S. Braesch-Andersen, R. J. Noelle, I. Stamenkovic, J. A. Ledbetter, A. Aruffo, The human T cell antigen gp39, a member of the TNF gene family, is a ligand for the CD40 receptor: Expression of a soluble form of gp39 with B cell co-stimulatory activity. *EMBO J.* **11**, 4313–4321 (1992).
80. L. E. Haswell, M. J. Glennie, A. Al-Shamkhani, Analysis of the oligomeric requirement for signaling by CD40 using soluble multimeric forms of its ligand, CD154. *Eur. J. Immunol.* **31**, 3094–3100 (2001).
81. V. P.-Y. Ma, Y. Hu, A. V. Kellner, J. M. Brockman, A. Velusamy, A. T. Blanchard, B. D. Evavold, R. Alon, K. Salaita, The magnitude of LFA-1/ICAM-1 forces fine-tune TCR-triggered T cell activation. *Sci. Adv.* **8**, eabg4485 (2022).
82. F. Kong, A. J. García, A. P. Mould, M. J. Humphries, C. Zhu, Demonstration of catch bonds between an integrin and its ligand. *J. Cell Biol.* **185**, 1275–1284 (2009).
83. W. Chen, J. Lou, C. Zhu, Forcing switch from short- to intermediate- and long-lived states of the alphaA domain generates LFA-1/lCAM-1 catch bonds. *J. Biol. Chem.* **285**, 35967–35978 (2010).
84. V. F. Fiore, L. Ju, Y. Chen, C. Zhu, T. H. Barker, Dynamic catch of a Thy-1–$\alpha_5\beta_1$+syndecan-4 trimolecular complex. *Nat. Commun.* **5**, 4886 (2014).
85. Y. I. Choi, J. S. Duke-Cohan, W. Chen, B. Liu, J. Rossy, T. Tabarin, L. Ju, J. Gui, K. Gaus, C. Zhu, E. L. Reinherz, Dynamic control of β1 integrin adhesion by the plexinD1-sema3E axis. *Proc. Natl. Acad. Sci. U.S.A.* **111**, 379–384 (2014).
86. F. Rosetti, Y. Chen, M. Sen, E. Thayer, V. Azcutia, J. M. Herter, F. W. Luscinskas, X. Cullere, C. Zhu, T. N. Mayadas, A lupus-associated mac-1 variant has defects in integrin allostery and interaction with ligands under force. *Cell Rep.* **10**, 1655–1664 (2015).
87. A. Elosegui-Artola, R. Oria, Y. Chen, A. Kosmalska, C. Pérez-González, N. Castro, C. Zhu, X. Trepat, P. Roca-Cusachs, Mechanical regulation of a molecular clutch defines force transmission and transduction in response to matrix rigidity. *Nat. Cell Biol.* **18**, 540–548 (2016).
88. Y. Chen, H. Lee, H. Tong, M. Schwartz, C. Zhu, Force regulated conformational change of integrin αVβ3. *Matrix Biol.* **60-61**, 70–85 (2017).
89. Y. Chen, L. A. Ju, F. Zhou, J. Liao, L. Xue, Q. P. Su, D. Jin, Y. Yuan, H. Lu, S. P. Jackson, C. Zhu, An integrin αIIbβ3 intermediate affinity state mediates biomechanical platelet aggregation. *Nat. Mater.* **18**, 760–769 (2019).
90. R. J. Mallis, K. Bai, H. Arthanari, R. E. Hussey, M. Handley, Z. Li, L. Chingozha, J. S. Duke-Cohan, H. Lu, J.-H. Wang, C. Zhu, G. Wagner, E. L. Reinherz, Pre-TCR ligand binding impacts thymocyte development before αβTCR expression. *Proc. Natl. Acad. Sci. U.S.A.* **112**, 8373–8378 (2015).
91. D. Banik, M. Hamidinia, J. Brzostek, L. Wu, H. M. Stephens, P. A. MacAry, E. L. Reinherz, N. R. J. Gascoigne, M. J. Lang, Single molecule force spectroscopy reveals distinctions in key biophysical parameters of αβ T-cell receptors compared with chimeric antigen receptors directed at the same ligand. *J. Phys. Chem. Lett.* **12**, 7566–7573 (2021).
92. H. Nishi, K. Furuhashi, X. Cullere, G. Saggu, M. J. Miller, Y. Chen, F. Rosetti, S. L. Hamilton, L. Yang, S. P. Pittman, J. Liao, J. M. Herter, J. C. Berry, D. J. DeAngelo, C. Zhu, G. C. Tsokos, T. N. Mayadas, Neutrophil FcγRIIA promotes IgG-mediated glomerular neutrophil capture via Abl/Src kinases. *J. Clin. Invest.* **127**, 3810–3826 (2017).
93. J. Fan, J. Shi, Y. Zhang, J. Liu, C. An, H. Zhu, P. Wu, W. Hu, R. Qin, D. Yao, X. Shou, Y. Xu, Z. Tong, X. Wen, J. Xu, J. Zhang, W. Fang, J. Lou, W. Yin, W. Chen, NKG2D discriminates diverse ligands through selectively mechano-regulated ligand conformational changes. *EMBO J.* **41**, e107739 (2022).
94. Y. Feng, K. N. Brazin, E. Kobayashi, R. J. Mallis, E. L. Reinherz, M. J. Lang, Mechanosensing drives acuity of αβ T-cell recognition. *Proc. Natl. Acad. Sci. U.S.A.* **114**, E8204–E8213 (2017).
95. D. K. Das, R. J. Mallis, J. S. Duke-Cohan, R. E. Hussey, P. W. Tetteh, M. Hilton, G. Wagner, M. J. Lang, E. L. Reinherz, Pre-T cell receptors (Pre-TCRs) leverage Vβ complementarity determining regions (CDRs) and hydrophobic patch in mechanosensing thymic self-ligands. *J. Biol. Chem.* **291**, 25292–25305 (2016).
96. L. V. Sibener, R. A. Fernandes, E. M. Kolawole, C. B. Carbone, F. Liu, D. McAffee, M. E. Birnbaum, X. Yang, L. F. Su, W. Yu, S. Dong, M. H. Gee, K. M. Jude, M. M. Davis, J. T. Groves, W. A. Goddard, J. R. Heath, B. D. Evavold, R. D. Vale, K. C. Garcia, Isolation of a structural mechanism for uncoupling T cell receptor signaling from peptide-MHC binding. *Cell* **174**, 672–687.e27 (2018).
97. P. Wu, T. Zhang, B. Liu, P. Fei, L. Cui, R. Qin, H. Zhu, D. Yao, R. J. Martinez, W. Hu, C. An, Y. Zhang, J. Liu, J. Shi, J. Fan, W. Yin, J. Sun, C. Zhou, X. Zeng, C. Xu, J. Wang, B. D. Evavold, C. Zhu, W. Chen, J. Lou, Mechano-regulation of peptide-MHC class I conformations determines TCR antigen recognition. *Mol. Cell* **73**, 1015–1027.e7 (2019).
98. X. Zhao, E. M. Kolawole, W. Chan, Y. Feng, X. Yang, M. H. Gee, K. M. Jude, L. V. Sibener, P. M. Fordyce, R. N. Germain, B. D. Evavold, K. C. Garcia, Tuning T cell receptor sensitivity through catch bond engineering. *Science* **376**, eabl5282 (2022).
99. M. H. Jo, P. Meneses, O. Yang, C. C. Carcamo, S. Pangeni, T. Ha, Determination of single-molecule loading rate during mechanotransduction in cell adhesion. *Science* **383**, 1374–1379 (2024).
100. V. P.-Y. Ma, Y. Liu, L. Blanchfield, H. Su, B. D. Evavold, K. Salaita, Ratiometric tension probes for mapping receptor forces and clustering at intermembrane junctions. *Nano Lett.* **16**, 4552–4559 (2016).
101. J. Banchereau, F. Briere, C. Caux, J. Davoust, S. Lebecque, Y.-J. Liu, B. Pulendran, K. Palucka, Immunobiology of dendritic cells. *Annu. Rev. Immunol.* **18**, 767–811 (2000).
102. J. P. Ridge, F. Di Rosa, P. Matzinger, A conditioned dendritic cell can be a temporal bridge between a $CD4^+$ T-helper and a T-killer cell. *Nature* **393**, 474–478 (1998).
103. S. R. M. Bennett, F. R. Carbone, F. Karamalis, R. A. Flavell, J. F. A. P. Miller, W. R. Heath, Help for cytotoxic-T-cell responses is mediated by CD40 signalling. *Nature* **393**, 478–480 (1998).
104. S. P. Schoenberger, R. E. M. Toes, E. I. H. van der Voort, R. Offringa, C. J. M. Melief, T-cell help for cytotoxic T lymphocytes is mediated by CD40–CD40L interactions. *Nature* **393**, 480–483 (1998).
105. Y. Chen, B. Liu, L. Ju, J. Hong, Q. Ji, W. Chen, C. Zhu, Fluorescence biomembrane force probe: Concurrent quantitation of receptor-ligand kinetics and binding-induced intracellular signaling on a single cell. *J. Vis. Exp.* e52975 (2015).
106. L. Ju, C. Zhu, Benchmarks of biomembrane force probe spring constant models. *Biophys. J.* **113**, 2842–2845 (2017).
107. D. T. Grob, N. Wise, O. Oduwole, S. Sheard, Magnetic susceptibility characterisation of superparamagnetic microspheres. *J. Magn. Magn. Mater.* **452**, 134–140 (2018).
108. Z. Yu, D. Dulin, J. Cnossen, M. Köber, M. M. Van Oene, O. Ordu, B. A. Berghuis, T. Hensgens, J. Lipfert, N. H. Dekker, A force calibration standard for magnetic tweezers. *Rev. Sci. Instrum.* **85**, 123114 (2014).
109. H.-K. Choi, H. G. Kim, M. J. Shon, T.-Y. Yoon, High-resolution single-molecule magnetic tweezers. *Annu. Rev. Biochem.* **91**, 33–59 (2022).
110. J. Lipfert, X. Hao, N. H. Dekker, Quantitative modeling and optimization of magnetic tweezers. *Biophys. J.* **96**, 5040–5049 (2009).

Acknowledgments: We thank C. Kim for help in cloning the CD40L constructs and S. Goudy for assistance in obtaining human tonsil tissues. **Funding:** This work was supported by National Institutes of Health grants U01CA250040 (to C.Z.), U01CA280984 (to A.S. and C.Z.),

R01CA238745 (to A.S.), and R01CA266052 (to A.S.); The Hyper IgM Foundation AWD-004331 (to C.Z.); Deutsche Forschungsgemeinschaft (DFG, German Research Foundation) SFB TRR 274, project A08 (to M.M., R.G., and J.W.); National Research Foundation of Korea (NRF) grant RS-2024-00337196 (to H.-K.C.); and Yonsei University Research Fund 2024-22-0036 (to H.-K.C.).
Author contributions: Conceptualization: H.-K.C., S.T., C.Z., A.S., and J.W. Methodology: H.-K.C., S.T., M.M., R.G., Z.Z., J.L., D.M.R.-A., C.Z., J.W., and A.S. Investigation: H.-K.C. and S.T. Visualization: H.-K.C. and S.T. Funding acquisition: H.-K.C., J.W., A.S., and C.Z. Project administration: C.Z. Writing—original draft: H.-K.C., S.T., and C.Z. Writing—review and editing: H.-K.C., S.T., M.M., J.W., A.S., and C.Z. **Competing interests:** The authors declare that they have no competing interests.

Data and materials availability: All data needed to evaluate the conclusions in the paper are present in the paper and/or the Supplementary Materials. Source data are provided with this paper. All codes used in this study for analysis are presented at Zenodo (doi.org/10.5281/zenodo.10929702). Analysis procedures are described in Materials and Methods.

Submitted 26 October 2023
Accepted 16 October 2024
Published 15 November 2024
10.1126/sciadv.adl5815